Contents

Synrad 1.4 algorithm

Marton Ady*

March 3, 2016

Extract from the PhD thesis *Monte Carlo simulations of ultra high vacuum and synchrotron radiation for particle accelerators[1]*

1 Introduction

The first version of Synrad+, a tool to simulate synchrotron radiation (SR) in accelerators, was created by R. Kersevan in the 1990s[2], building on the codebase of MOLFLOW[1]: instead of tracing molecules, it traced virtual photons and could visualize the flux distribution in the 3D geometry. Using the original codebase, I have modernized it, both in terms of graphical interface and by optimizing the photon generation algorithm. While doing this, priority was given to ensure compatibility with Molflow+ presented in the previous chapter: both programs can read each other's file formats, and this new simulator - renamed to Synrad+ - is intended to be used as part of a package helping to calculate the SR-induced dynamic gas load for vacuum simulations.

Our synchrotron radiation simulations go along the following steps, each detailed later:

- The user defines the optics and the beam parameters of the machine

- The source of the synchrotron radiation, *magnetic regions* are calculated

- Virtual photons are generated from these sources

- Ray-tracing is performed until photons leave the system or are absorbed:

    - Collisions are found with the chamber wall and photons are absorbed or reflected

    - Treating the wall chamber as a smooth or rough surface, reflected photons get a new direction

- Results are computed, then visualized within the program or exported for post-processing

2 Defining magnetic regions

To generate photons, we require at least one source. We could choose from several possibilities for defining it, depending on what we request as input from the user and what we calculate internally.

Usually an engineer performing a SR simulation knows the beam parameters and the optics of a machine, therefore in Synrad+ instead of the complete beam trajectory - we ask the user to set up a so-called magnetic region: a volume where the magnetic field is known at every point. This magnetic field can be defined either directly (coordinate-wise, using either absolute or beam length coordinates), or by describing common optics elements. Supported elements include:

- Dipoles

- Quadrupoles

- Analytic magnetic fields (for helicoidal, sinusoidal or other periodic structures)

When using these elements, their macroscopic properties (size, strength, orientation) are input by the user and the magnetic field is calculated within Synrad+.

---

*CERN, marton.ady@cern.ch

[1]MOLFLOW is the original UHV simulator written by R.Kersevan in the 1990s, and the modern version is intended to be distinguished by being renamed to Molflow+

Table 1: Quadrupole parameters in Synrad+

α	Z angle with real-world XZ plane (pos. towards Y)
β	Z angle with real-world YZ plane (neg. towards X)
rot	quadrupole focusing plane rotation around Z respective to X
K	Dipole strength, in T/m

- In case of dipoles, the magnetic field is constant.

- For periodic structures, such as wigglers, helicoidal and sinusoidal elements, the description is analytic.

- As for quadrupoles, to determine a points magnetic field, we transform the real-world X, Y, Z coordinates of the point into the quadrupoles own coordinate system. If Z' is the quads axis, and X' and Y' point from the center of its entrance to the standard quadrupole focusing/defocusing directions (in center between the southern and northern magnet poles), we define the parameters in Table 1, shown in Fig.1:

  First we transform the P point coordinates to the quadrupoles own coordinate system.[2]

  Then, with the P'_x and P'_y local coordinates obtained, we can express the magnetic field in the quads coordinate system: if the point is inside the quadrupole of length L ($0 < P'_z < L$), then

$$B'_x = -K \cdot P'_y$$

$$B'_y = -K \cdot P'_x$$

$$B'_z = 0$$

  otherwise the magnetic field is 0.

  Then we get the real-world magnetic field coordinates by an inverse transformation.[3]

Apart from the magnetic field, we need the following properties for a fully defined source:

- Start position and starting direction of the beam at the first point of the region

- Region limits

- Beam properties, such as:

---

[2] We calculate the offset of P compared to the quadrupole's entrance:

$$dX = x_P - x_{\text{center}}$$

$$dY = y_P - y_{\text{center}}$$

$$dZ = z_P - z_{\text{center}}$$

Then we transform P coordinates to those of the quadrupole:

$$P''_x = dX * \cos(\beta) + dZ * sin(\beta)$$

$$P''_y = -dX * \sin(\alpha) * \sin(\beta) + dY * \cos(\alpha) + dZ * \sin(\alpha) * \cos(\beta)$$

$$P'_z = -dX * \cos(\alpha) * \sin(\beta) - dY * \sin(\alpha) + dZ * \cos(\alpha) * \cos(\beta)$$

$$P'_x = P''_x * \cos(rot) + P''_y * \sin(rot)$$

$$P'_y = -P''_x * \sin(rot) + P''_y * \cos(rot)$$

[3] To get the B_x,B_y,B_z coordinates from B'_x,B'_y,B'_z:

$$B''_x = B'_x * \cos(rot) - B'_y * \sin(rot)$$

$$B''_y = B'_x * sin(rot) + B'_y * \cos(rot)$$

$$B''_z = B'_z$$

$$B_x = B''_x * \cos(\beta) - B''_y * \sin(\alpha) * \sin(\beta) - B''_z * \cos(\alpha) * \sin(\beta)$$

$$B_y = B''_y * \cos(\alpha) - B''_z * \sin(\alpha)$$

$$B_z = B''_x * \sin(\beta) + B''_y * \sin(\alpha) * \cos(\beta) + B''_z * \cos(\alpha) * \cos(\beta)$$
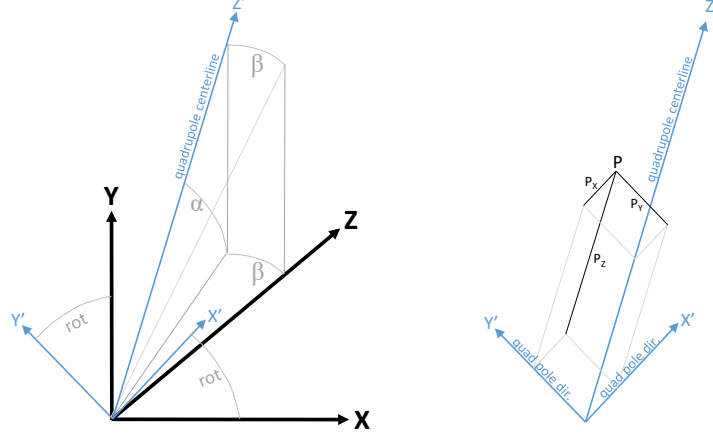
Figure 1: Left: quadrupole coordinate systems α, β, rot angle definition
Right: point definition in quadrupoles coordinates

- – Particle type
- – Energy
- – Current

- • We can assume that a beam is ideal (has no width), otherwise we define:

  - – Emittance
  - – Horizontal/vertical coupling
  - – Energy spread
  - – The Beta and horizontal dispersion (Eta) functions, coordinate-wise

We use the **dipole approximation**: we consider the beam as a succession of tiny dipoles, each having its own direction and curvature. The advantage is that the resulting synchrotron radiation can be relatively easily described analytically, and a fast photon generation algorithm can be implemented. At the same time, this approach isnt suitable for coherent sources such as undulators, where interference modifies the SR pattern substantially.

Starting from the first point in the region, our code calculates successive ones with the user-defined step length, until the region boundary is reached. For each new point, we calculate the following properties:

2.1 Location, curvature and beam direction

We first determine the Lorentz force:

$$\overline{F_L} = q\,\bar{v} \times \bar{B}$$

Then we calculate the curvature $\bar{\rho}$ using the practical formula [3][4]:

$$\bar{\rho}\,[m] = \frac{E\,[GeV]}{0.3 \cdot B_\perp\,[T]} \cdot \left\| \bar{F}_L \right\|$$

where

$$B_\perp = \sqrt{\left| B \right|^2 - B_\parallel^2} = \sqrt{\left| B \right|^2 - \left\| \bar{v} \right\| \bar{B}}$$

Then the offset dL to the next points position can be calculated as

$$\overline{dL} = dL.\bar{v}$$

and the next points direction $v*$ is obtained by rotating v around

$$\bar{O} = \bar{v} \times \bar{\rho}$$

---

[4] $\left\| \bar{F}_L \right\|$ stands for a unit length vector parallel to $\bar{F}_L$, while $\left| \bar{F}_L \right|$ is the length of $\bar{F}_L$
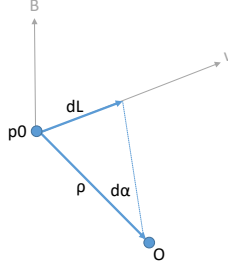
Figure 2: Notations for trajectory step calculation (in this figure we assumed a positive charge particle)

axis by

$$d\alpha \sim \frac{dL}{|\bar{\rho}|}$$

2.2 Beam width and divergence

We describe non-ideal beams probabilistically: when generating a photon at a given pre-calculated trajectory point, I choose the starting location with an offset in the plane perpendicular to the (local) beam direction. This offset follows a bivariate Gaussian distribution, with mean 0 and st.dev. σ_x and σ_y corresponding to the beam horizontal/vertical size, obtained as:

$$\epsilon_x = \frac{\epsilon}{1 + \text{coupling}}$$

$$\epsilon_y = \epsilon_x \cdot \text{coupling}$$

$$\sigma_x = \sqrt{\epsilon_x \cdot \beta_y + \left(\eta_x \cdot \frac{\Delta E}{E}\right)^2}$$

$$\sigma_y = \epsilon_y \beta_y$$

$$\sigma'_x = \sqrt{\frac{\epsilon_x}{\beta_y} + \left(\eta'_x \cdot \frac{\Delta E}{E}\right)^2}$$

$$\sigma'_y = \sqrt{\frac{\epsilon_y}{\beta_y}}$$

where $\frac{\Delta E}{E}$ is the energy spread, and σ'_x and σ'_y are the st.dev. of the photons directional divergence due to the beam width, added to the natural divergence of an ideal beam (see later).

At this point, we have our sources in the form of magnetic regions, consisting of a large number of pre-calculated trajectory points. In the dipole approximation each trajectory point can serve as short dipole source, individual from the others. In the real world, these dipoles generate a number of physical photons every second, the exact number depending on the magnetic field, the beam energy and the current. Our simulations are not time-dependent, so the flux from such a dipole source is considered constant. During our Monte Carlo simulations, we will generate virtual photons, distributed equally between these trajectory points.

When generating such a virtual photon, we need to determine the following properties:

- Energy

- Polarization

- Flux (the number of physical photons per second [5] it represents)

- Power (the SR power that this flux carries)

- Starting location and direction, as described earlier

These parameters arent independent of each other: for example, as the spectrum of SR is well defined; choosing a different photon energy will change the flux the virtual photon represents. To determine the exact relation between these properties, we need to recall the analytic description of SR.

---

[5] Usually for Monte Carlo simulations each virtual particle represents a given number of physical ones. In our case, as the photon flux is constant, each generated virtual photon corresponds to a certain flux, not an absolute number of photons
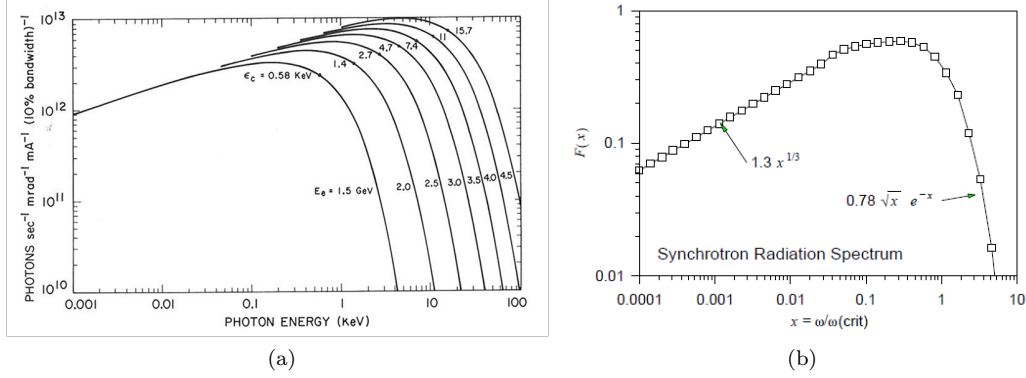
Figure 3: Synchrotron radiation spectrum, on absolute (3a) and relative (3b) scales
Source: [5] (for 3a) and [6] (for 3b)

3 Synchrotron radiation properties

3.1 Spectrum

Synchrotron radiation consists of photons of different energy: its wide spectrum is one of the main advantages of synchrotron light sources. The spectrum of a dipole can be described analytically. If γ is the relativistic factor (depending on the beam energy), ρ is the radius of curvature (depending on the magnetic field strength), then for wavelength λ, we will have the following number of photons per second [4]:

$$N\left(\lambda, t\right) = \frac{3^{3/2}}{4\pi} \frac{e^2 \gamma^4}{h\rho^2} \left(\frac{\lambda_c}{\lambda}\right)^2 \int_y^\infty K_{5/3}\left(\eta\right) d\eta \tag{1}$$

per unit $d\lambda$, where $K_{5/3}$ is a modified Bessel function. Such spectrums are plotted in Fig.3a.

The expression includes the energy dependence through parameter $y = \frac{\lambda_c}{\lambda}$ (equal to E/E_c since the energy and the wavelength can be converted to each other through equations $E = hf$ and $c = \lambda f$). Because of this, it is convenient to express the spectrum on a relative energy scale, in units of critical energy E_c [6]. If we plot this relative spectrum on log-log scale (Fig.3b), we can notice that its low-energy tail is straight ($N \sim 1.3 * x^{1/3}$), and it has a high-energy cutoff before $E = 10 * E_c$.

3.1.1 Fluxwise/powerwise generation

Even if we know the distribution of the SR energy, virtual photons can represent any number of physical photons, so when we begin our Monte Carlo simulation, we still have the freedom to sample the spectrum arbitrarily. We could, for example, generate virtual photons distributed evenly in a certain energy range, or we could oversample energies with high photon flux (fluxwise generation), or concentrate on high energy photons that carry most of the energy (powerwise generation). Choosing the correct strategy depends on the task we need to solve.

Traditionally, SR calculations for engineering tasks concentrate on the SR power: when designing chamber walls, absorbers and shielding, the thermal load can cause permanent damage, therefore detailed simulations and an adequate cooling design is necessary.

If we are only interested in the heat load, it is therefore recommended to generate photons powerwise, omitting low-energy photons. For example, limiting the generated photon energy to $0.1\,E_c$ .. $20\,E_c$ contains more than 95% of the total power, whereas this range contains less than half of the photons (speeding up a possible heat load simulation by a factor of two). Moreover, as we will see later in this section, the high-energy part of SR is more collimated, and scatters with a lower probability, therefore simulations converge relatively fast.

In accelerator design, however, low-energy photons are very important. The reason is that while these photons carry less heat, even photons with energy as low as $4\,\text{eV}$ are able[7] to increase the dynamic gas load through photon stimulated desorption, as described in chapter ??.

---

[6]The critical energy is defined so that half the power of the SR is carried by photons with energy below it
[7]$4\,\text{eV}$ is an average photoelectric work function value for common metals
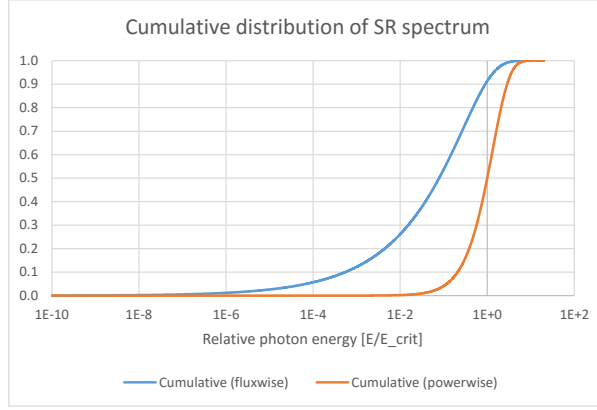
Figure 4: Cumulative distribution functions for synchrotron radiation

As low energy photons are distributed over a larger angle, and they scatter more easily, they are able to reach farther parts of an accelerator, where traditional heat load calculations show very little SR presence.

Considering the above, Synrad+ allows the user to choose between fluxwise and powerwise generation. If ran for a sufficiently long time, both methods will yield the same result, however as statistical accuracy increases with the number of traced virtual photons for heat load calculations, powerwise generation will converge faster, whereas fluxwise generation will concentrate on low-energy photons calculating the absorbed flux faster.

For both strategies, we generate photons using numerical inversion: at the beginning of a simulation, we sample the energy range between 1×10^{-10} E_c and 100 E_c on 5000 logarithmically increasing intervals. For each interval we calculate the number of photons and the power it contains[8]. Instead of the analytic expression 1 containing the integral $G_0(x) = \int_y^\infty K_{5/3}$, we use a fast numerical approximation method[7]. Summing these interval fluxes and powers, we construct one fluxwise and one powerwise cumulative distribution function for the whole energy range, shown in Fig.4.

Once these cumulative distributions are stored in memory, for each generated photon, we reverse look up uniformly generated random numbers and scale the interpolated (relative) photon energy with the critical energy of the actual trajectory point.[9]

Given the sampling at the beginning, the energy range $[10^{-10}..10^2]E_c$ presented above is the widest for which simulation is possible in Synrad. The user can narrow the generated photon range for speedup, though. In that case random numbers are generated only between the C.D.F. values of the lower and upper energy limits.

3.2 Representation

As mentioned earlier, all our SR simulations are steady-state, so each traced virtual photon represents a given SR flux. To assign a given physical flux and power to our virtual photons, we calculate the following way:

- The total SR flux for an electron beam of a full revolution in practical units is
  8.084×10^{17} *E[GeV]*I[mA] photons/sec [9]
  or 4.131×10^{14} *γ*I[mA] for a general particle, γ being the relativistic factor

- Each of our short dipole sources at the pre-calculated trajectory points represents a fraction of the full revolution:
  revolution_ratio=$dL/(2\rho\pi)$
  with dL the trajectory step length andρ the local radius of curvature

- We choose a starting point uniformly among the precalculated trajectory points. We would have a full scan when we have chosen each starting point exactly once. As we choose starting points

---

[8]The power is the number of photons in the interval multiplied by the mean interval energy

[9]It is worth mentioning that one author has analytically approximated[8] the inverse of these C.D.F. functions by splitting the energy range to three intervals, then expressing the inverse functions with a combination of regular and Chebyshev polynomials with approximately 30 coefficients in each interval. That method allows direct generation of the spectrum.
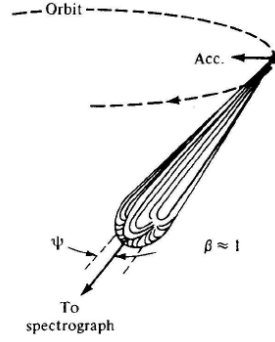
Figure 5: Illustration of Synchrotron Radiation in the laboratory frame.
Source: fig.3. of [11], based on [12]

randomly, we can express a full scan in statistical terms as having generated the same number of test photons as the number of trajectory points. At this point, the number of scans will be 1. In general, we can introduce the factor

$\#_{scans} = \frac{\#_{generated\ test\ photons}}{\#_{trajectory\ points}}$

- Having all the quantities above, in case of fluxwise generation, one test photon will represent

$$K_{\text{real/virtual}} = \text{revolution\_ratio} * \gamma * 4.131 \times 10^{14} * I[mA]/\#_{\text{scans}} \qquad (2)$$

photons per second.

Remarks:

- The power each test particle represents is the flux calculated above, multiplied by the average photon energy for the whole SR spectrum [10]

- Consequently, if we generate test photons powerwise, the represented flux, calculated above, is divided by the average photon energy for the whole energy range

- As mentioned earlier, the user can limit the photon generation range to a narrower range than $[10^{-10}..10^2]E_c$. In this case two new factors are calculated, which describe what ratio of the full SR flux and power spectrum is contained in the limited energy range. The reverse lookup process for finding the photon energy and the representation above will be corrected by these factors. For simplicity these correction factors are omitted in this description.

3.3   Vertical distribution and polarization

Synchrotron radiation from an accelerated particle has the highest intensity towards the direction of the beam. The exact angular distribution depends on the particles energy, and is described by Schwingers equation[10]. A qualitative representation is seen in Fig.5.

Exactly 7/8 of the SR from a dipole is polarized parallel to the orbit plane[13], and 1/8 orthogonal to it. Because of this strong dominance of the parallel polarization, it is desirable to treat the two components separately. The ratio between the parallel and orthogonal planes depends on the vertical angle ψ between the observation point and the orbit plane.

The exact dependence can described analytically (eq. 13. of [4]). For a given vertical angle ψ and for a photon wavelength λ, the two components can be expressed:

At $\psi = 0$

$$F\left(\frac{\lambda_c}{2\lambda}, 0\right) = F_{\parallel}(0) = K_{2/3}^2\left(\frac{\lambda_c}{2\lambda}\right)$$

And generally at angle ψ

$$F_{\parallel}(\psi) = \left(1 + \gamma^2\psi^2\right) K_{2/3}^2\left[\frac{\lambda_c}{2\lambda}\left(1 + \gamma^2\psi^2\right)^{3/2}\right]$$

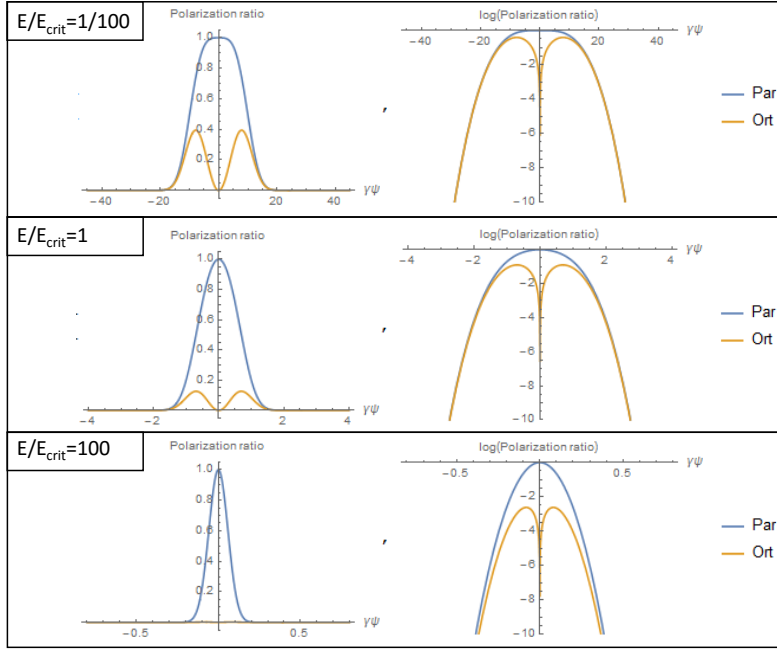[10] $E_{avg} = 0.308 E_c$ for the range $[10^{-10}..10^2]E_c$

8

Figure 6: Polarization components for different lambda ratios. Each plot has an X scale that depends on the relative photon energy:
$\gamma\psi = [-4/(E/E_c)^{0.35} .. + 4/(E/E_c)^{0.35}]$
Left: linear scale, Right: logarithmic scale

$$F_\perp(\psi) = \gamma^2\psi^2 \left(1 + \gamma^2\psi^2\right) K_{1/3}^2 \left[\frac{\lambda_c}{2\lambda}\left(1 + \gamma^2\psi^2\right)^{3/2}\right]$$

where $K_{1/3}$ and $K_{2/3}$ are modified Bessel functions. The solution of this analytic expression can be visualized (see Fig.6) on a relative scale where the vertical angle is expressed in units of γ, and with a different X axis range for each energy. Finally, we often use the expression *degree of polarization* which is defined as $P_{\text{lin}} = (F_\| - F_\perp)/(F_\| + F_\perp)$.

We can notice that in the plane of the orbit the polarization is purely linear.

As the modified Bessel functions can be approximated, one approach to generate photons according to this angular distribution would be to similar to the spectrum generation - construct the cumulative distribution function for vertical angles between 0 and $\pi/2$, as the function is symmetric (the first version of Synrad in the 1990s used that method). However, this is computationally expensive: we need to integrate a rather complex analytic expression for every generated photon.

I chose to numerically pre-calculate the integrals. However, several challenges need to be tackled to sample the distribution for a large range of energies.

In Fig.6 the curves for the different energies are similar, but not the same: I did not find a convenient yet precise scaling method to derive all distributions from a single stored one, therefore I decided to sample them for all energies.

We can see that the sampling must be performed on an angular range that depends on the energy (corresponding to the fact that SR is more collimated for high energies). I have chosen to include all the angles where the radiated flux is larger than 10^{-10}th of the peak. I have found that setting this sampling range to $\gamma\psi = [-4/(E/E_c)^{0.35} .. + 4/(E/E_c)^{0.35}]$ is adequate for the range $E/E_c =$[1E-10 .. 100], as shown on the surface plot 7.

Taking advantage of the symmetry of the distribution, I have sampled one half of these surfaces (individually for the two polarization components and also for their sum) the following way:

- Energy: Logarithmically in the range $E/E_c =$[1E-10 .. 100], along 121 values, with two consecutive values having the ratio of $10^{0.1} = 1.259$

- $\gamma\psi$: Linearly along 200 values from 0 to $4/(E/E_c)^{0.35}$, with $\Delta = 0.005 * 4/(E/E_c)^{0.35}$

- Post-processing: integrating and normalizing each line (corresponding to given E/E_c values), to get a cumulative distribution function
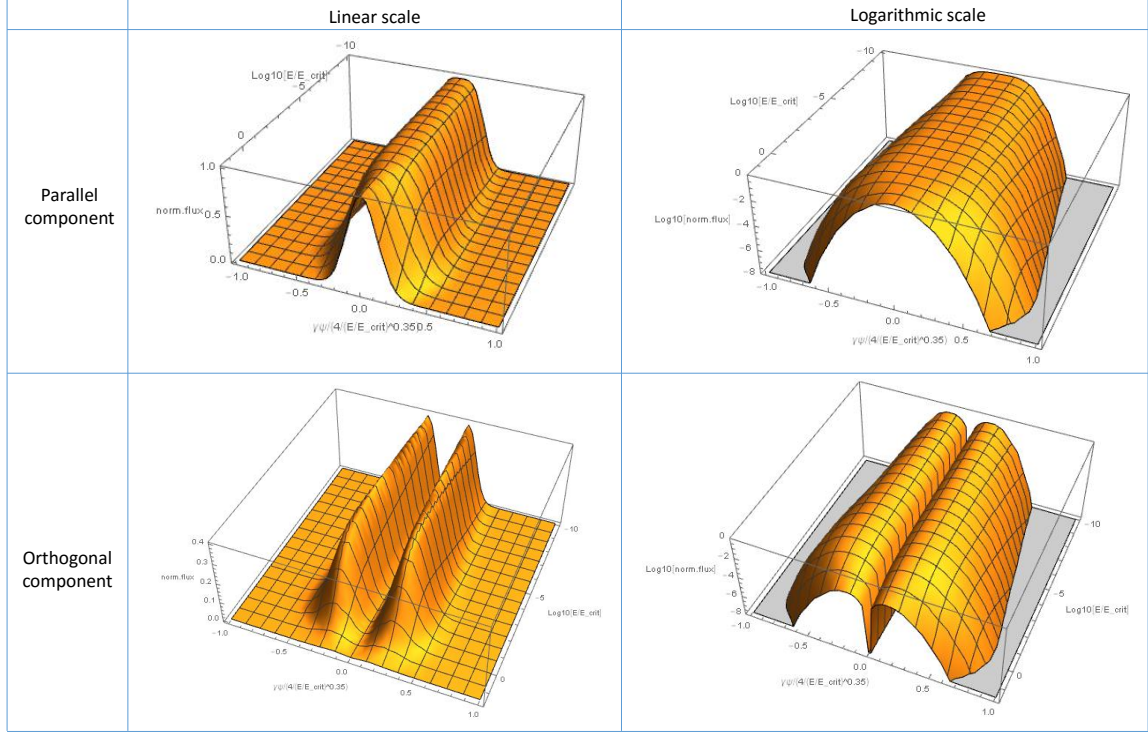
9

Figure 7: Flux distribution for the parallel (top) and orthogonal (bottom) polarization components, as a function of the relative photon energy and the vertical angle. Please note that the angle range is normalized for each energy between $\gamma\psi = [-4/(E/E_c)^{0.35} .. + 4/(E/E_c)^{0.35}]$

And stored the resulting three tables of 121x201 values as input files, loaded at each startup of Synrad.

3.4 Horizontal distribution

Although information regarding the vertical distribution of SR from a dipole is abundant in literature, and experimental measurement is straightforward (for example, using a photosensitive film after a collimator), less information is available on the horizontal distribution: to measure it, we would require a sufficiently short dipole source, where the beam rotation is small compared to the horizontal distribution. As Synrad treats the beam as a succession of such tiny dipoles, we need the angular description of such short sources. We refer to [14] which derives the angular distribution from the far field expression of a point charge. The analytic solution presented there for the field strength of the two polarization components is:

$$f_\parallel = \left(1 + \gamma^2\theta^2\right)^{-3} \cdot \left(1 - \gamma^2\theta^2 + 2\gamma^2\theta^2 \sin^2\phi\right)$$

$$f_\perp = -2\left(1 + \gamma^2\theta^2\right)^{-3} \cdot \gamma^2\theta^2 \sin\varphi\cos\varphi$$

and the intensity (flux) is the square of these. The expressions use the angles ϕ (elevation angle of the observation point relative to the orbit plane) and θ (angle between the local beam direction and the observation point), as shown on Fig.8, expressed in terms of ψ (vertical) and χ (horizontal) angles.

Similar to the vertical distribution, instead of evaluating the analytic expressions containing 11 trigonometric and 15 power expressions for every generated photon, I can achieve a significant speedup by pre-calculating and sampling the distribution.

Luckily for our case, the divergence of SR scales with $1/\gamma$, therefore the 2-dimensional horizontal/vertical distribution can be stored on a relative scale where the angles are expressed in units of $\gamma\psi$ and $\gamma\chi$.

The distributions are symmetric both in horizontal and vertical directions (in the analytic expressions angles are arguments of even trigonometric functions or are raised to squares), therefore it is sufficient to evaluate only the first (positive) quarter of the full range. As shown in Fig.9, the parallel component is peaked at $(\psi, \chi) = (0, 0)$, whereas the orthogonal exhibits a peak with an offset, creating four orthogonal lobes around the beam direction in the SR pattern.
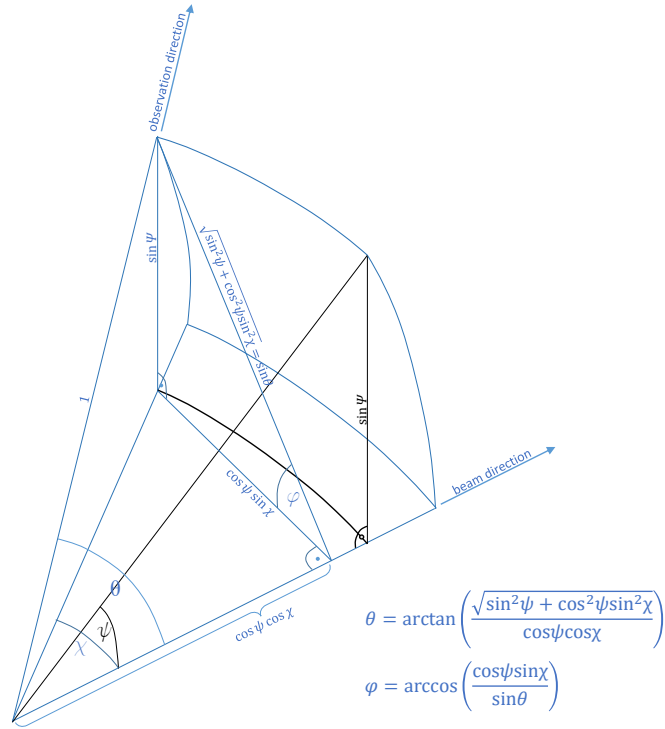
10

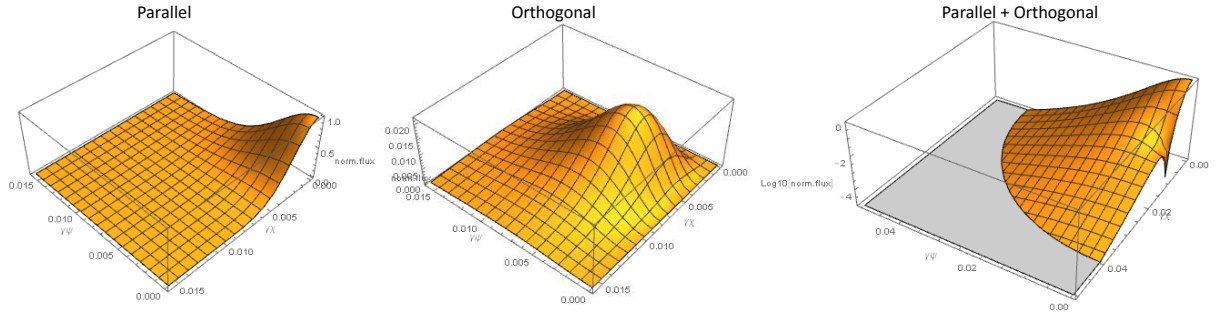Figure 8: Angular notations used in the expression for the horizontal SR distribution from a short dipole

Figure 9: Horizontal/vertical distributions of SR components originating from a short dipole for $\gamma = 100$, normalized to the peak flux at $(\psi, \chi) = (0, 0)$

In Fig.9 (right) the sum of the two components is plotted on a logarithmic scale, revealing the "dip" on the horizontal axis, which is also visible in Fig.14 (bottom right).

The problem with sampling these distributions is that they extend to a very large angular range (in theory the full hemisphere around the beam direction), but their peak is contained in a very small solid angle. Omitting larger angles where the distribution has small values is not an option: for any generated vertical angle we need Synrad+ to be able to generate a valid horizontal distribution, so every "line" (fixed $\psi\gamma$ value) of the digitized 2D map needs to have precise values in order to construct a cumulative distribution function.

In practice, we can limit the sampled range, if we decide that as before the lowest photon energy that we generate (which will have the largest angular divergence) will be $E_{\text{lowest}} = 10^{-10} E_c$

With the vertical angle limited to $4 * E/E_c^{0.35}$, and $E/E_c = 1 \times 10^{-10}$ in this worst case, we get the largest angle, in units of gamma, as $\psi_{max} * \gamma \sim 12500$. Since as seen in Fig.10, the vertical and horizontal distribution has more or less the same range, for simplicity, we will for both angles sample between 0 and $10000/\gamma$. This sampling will need to concentrate on the very limited peak near $(\psi, \chi) = 0, 0$, but at the same time contain values for all the range, therefore a logarithmic sampling is convenient (illustrated in Fig.10).

I have stored this angular distribution in three tables (parallel and orthogonal polarization and their sum), as follows:
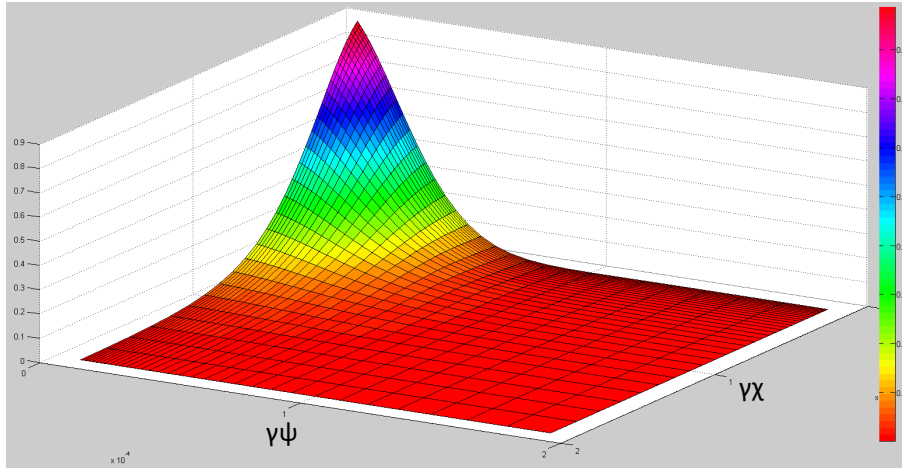
Figure 10: Logarithmic sampling of the directional distribution of SR, with sampling focusing on the narrow peak

- Vertical/horizontal angles, in units of $1/\gamma$: from 0 to 10000, sampled in 176 logarithmically increasing intervals (so that the ratio of two consecutive intervals is 1.0965)

- For each ψ vertical angle, the distribution is integrated on the range of χ values then normalized, constructing therefore 176 cumulative distribution functions. (At the integration care must be taken that the integration interval increases logarithmically)

4 Photon generation process

Having the energy, vertical and horizontal distributions in the memory, the exact photon generation algorithm goes along the following steps:

4.1 Source point choice

During a simulation, as described earlier, SR sources are represented as magnetic regions, each storing the ideal beam trajectory as a series of short dipoles. Among these trajectory points, one is chosen randomly.[11]

If the user wishes to approximate the beam as ideal, we can use the position, direction, curvature vectors and the critical energy stored in memory during the trajectory calculation. If, however, the beams emittance is also taken into account, the pre-calculated position is offset according to two Gaussian distributions describing the beam width. Depending on the type of the SR source, a position offset can change the magnetic field (in case of a quadrupole, for example), in which case the magnetic field vector is recalculated and the curvature and critical energy are updated.

4.2 Choosing photon energy

Depending whether the user generates virtual photons flux- or powerwise, one of the two stored cumulative distribution functions describing the SR spectrum is used for a reverse interpolation. The resulting relative energy is converted to absolute by multiplying with the local critical energy.

4.3 Choosing vertical angle

The photons "natural" vertical angle is generated the following way:

Knowing the relative photon energy (E/E_c) from the previous step, in the preloaded vertical angle / energy distribution from section 3.3 the two lines digitized for the energies just below and above the searched energy are looked up by binary search.

---

[11] I have found that it is slower to interpolate the photon starting positions and beam / magnetic field properties between the trajectory points, than to reduce the step length, and use more of these pre-calculated locations as photon starting points. To give an approximate order of magnitude, it is suitable to model a simple dipole with 10.000 points, and not to have more than a total of 1.000.000 trajectory points for all regions of the model.
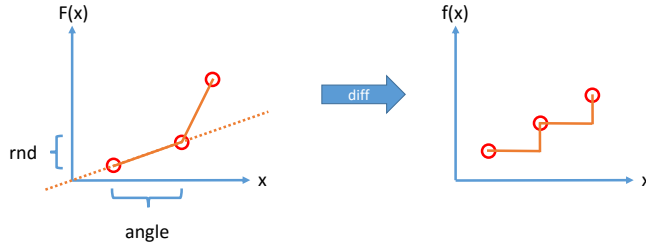
Figure 11: Looking up a random number rnd in an angular C.D.F., linear interpolation will result in a step p.d.f. function
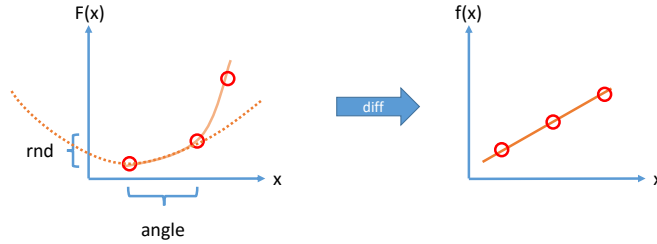

Figure 12: Quadratic interpolation in the C.D.F. results in a continuous p.d.f.

From the values of the cumulative distribution functions stored in these two lines (for a slightly lower and slightly higher energy), an interpolated distribution is calculated for the searched energy.

Then a reverse interpolation is performed in this new distribution constructed on-the-fly, to assign a vertical angle to a pseudo-random number. If the beam's emittance isn't considered to be zero, this natural vertical angle is offset by a σ'_y width Gaussian-distributed random number, to account for the divergence.

4.4 Choosing horizontal angle

Similar to the previous step, the generated vertical angles lower and higher neighbors are looked up in the angular distribution table described in section 3.4, an interpolated C.D.F. is constructed, then a pseudo-random number is reverse interpolated to find the corresponding horizontal angle.

If the beam isn't ideal, this natural horizontal angle is then also offset with a σ'_x width Gaussian-distributed random number.

4.5 Reverse interpolating in a cumulative distribution function

During the photon generation process, we apply the numerical inversion method three times: we look up a random number in a cumulative distribution function for the photon energy, then for the vertical and the horizontal angles. I have experienced that for numerical inversion, linear interpolation is not the most efficient method: if we assume that the C.D.F. is linear between the sampled points, then it will correspond to a step function in the probability distribution function, illustrated in Fig.11.

This will result in discontinuity in the generated distributions, which we could compensate by increasing the number of sampled points. This, however, increases both the memory requirement and the steps required for the binary lookup. For larger tables, especially the vertical/horizontal angle distribution, the sample size can be significantly reduced (without a noticeable change in the generated distributions) by using quadratic interpolation, which takes into account adjacent points to make the first derivative of the C.D.F. continuous, corresponding to a continuous p.d.f. This is illustrated in Fig.12.

The forward quadratic interpolation (looking up a y value at a given x location) is a well-established problem: for three data points $(x_1, y_1), (x_2, y_2), (x_3, y_3)$, the interpolated $y = P(x)$ value and the $y' = P'(x)$ derivative can be expressed by the Lagrange interpolating polynomials:
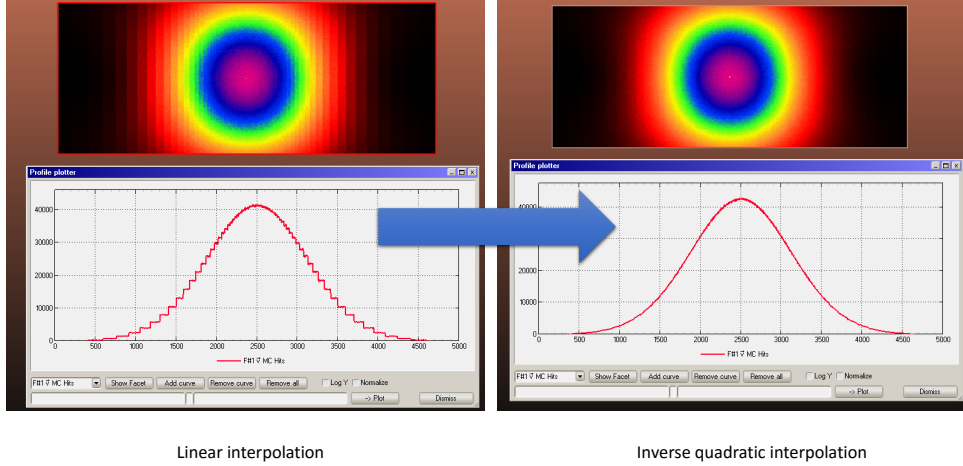
Figure 13: Comparison of the linear (left) and inverse quadratic (right) interpolation methods, for the same number of sampled points

$$P(x) = \frac{(x-x_2)(x-x_3)}{(x_1-x_2)(x_1-x_3)}y_1 + \frac{(x-x_1)(x-x_3)}{(x_2-x_1)(x_2-x_3)}y_2 + \frac{(x-x_1)(x-x_2)}{(x_3-x_1)(x_3-x_2)}y_3 \tag{3}$$
$$P'(x) = \frac{2x-x_2-x_3}{(x_1-x_2)(x_1-x_3)}y_1 + \frac{2x-x_1-x_3}{(x_2-x_1)(x_2-x_3)}y_2 + \frac{2x-x_1-x_2}{(x_3-x_1)(x_3-x_2)}y_3$$

We, however, do the inverse: we look for the x value corresponding to a y value. Therefore we solve the above equation for x, which will result in two roots[12], one of which – in our interest – will be between x_1 and x_2. The improvement in the generated distribution - with the same number of sampled points - is illustrated in Fig.13.

Compared to generating photons by evaluating the analytic expressions, this sampling and reverse interpolation method results in a speedup of more than 10x (see Fig.14).

4.6 Validity

The photon generation algorithm described earlier (without my optimizations) has been used in multiple MC simulators including GEANT4[15], MAD-X[16], and its validity is discussed in many places of literature, of which a good summary is published in chapter 1.3 of [8]. Briefly:

- In reality, the spectrum is not continuous as we assume but discrete. However, for accelerator applications the mode number will be too high to make this noticeable (n_c =1E13 for 10 GeV electrons)

- The spectrum is valid as long as the photon energy is small compared to the particle energy, which is safe to assume for electron beams in modern (GeV) accelerators

- It assumes a homogenous magnetic field for each trajectory point, omitting edge effects of short dipoles

- It does not include coherence effects of short bunches with many particles

As for my implementation, it can be tested against calculated data for real machines. Based on [17], I can analytically calculate the spectra for a bending magnet and a wiggler of the Brookhaven National Laboratorys VUV Storage Ring, which – operating from 1981 - was one of the first 2nd generation light sources in the world. The referenced article gives a practical version of eq.1:

Flux(en)[photons/sec/0.1% bandwidth]=$N*\alpha$[mrad]*2.457E13*E[GeV]I[A]$G_1(en/E_c)$

where E_c is the critical energy, α is the horizontal bending angle, N is the number of wiggler half-periods (1 in case of a bending magnet), E is the beam energy, I the beam current and

---

[12]I solved eq. 3 for x with the symbolic solver Mathematica. The resulting expressions giving the two roots are too long to state here.
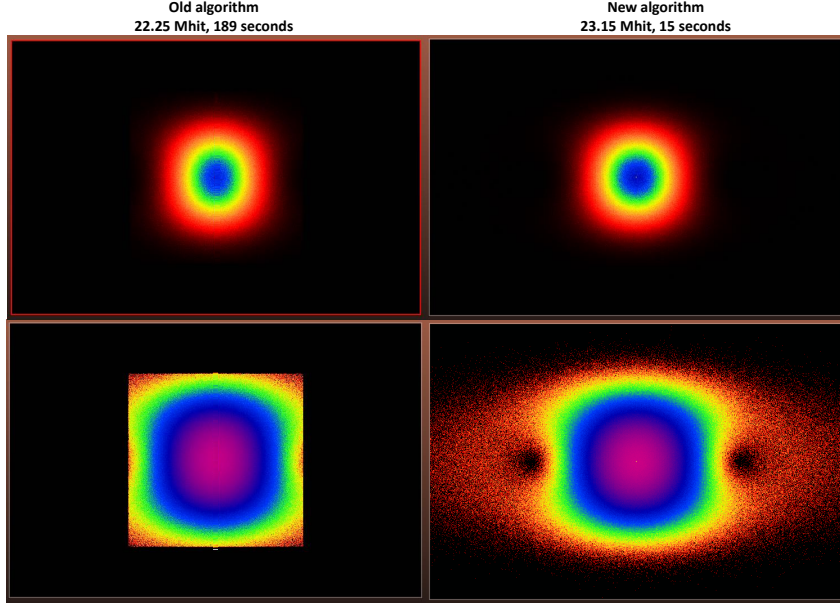
Figure 14: angular distributions for ~ 22 million fixed energy photons originating from a short dipole.
Left: generated by evaluating the analytic expressions (generated angles limited for speedup)
Right: generated by reverse lookup in sampled distributions

Table 2: Machine parameters of a dipole and a wiggler of the BNL VUV storage rings, as published in [17].

	VUV bending magnet	U13U wiggler
Beam	0.745 GeV, 800mA	
Magnetic field [T]	1.28	0.81 (max)
Radius of curvature [m]	1.91	3.06 (min)
Critical energy [eV]	472.3	298.8 (max)
Period length [mm]		100
2N (Half-periods)		45

$$G_1(y) = y \int\limits_y^\infty K_{5/3}(y')dy'$$

The article then integrates the SR light on a 5 mrad horizontal opening and publishes the resulting plots. Comparing my results to the analytically calculated examples test Synrad's beam trajectory calculation, photon energy and angular divergence calculation and ray tracing modules at the same time.

Parameters for the bending magnet designated as VUVBM and the wiggler referred to as U13U are summarized in Table2.

The magnetic regions in my simulation are described by 3000 points for the dipoles and 2200 points for the wiggler, and SR patterns are registered on two textures of 300x200 and 180x200 cells. The spectrum is vertically integrated on a 5 mrad wide opening. The simulation (Fig.15) took 1 minute on a standard desktop PC, during which 60 million test photons were generated.

Results, plotted in Fig.16 are compared to the analytic formula (also plotted in Fig.1. of the original article [17]), and show a very good match. [13]

---

[13] The simulated flux results for the wiggler are slightly lower than the analytic calculations. It turns out that when using a collimator to filter for 5 mrad angle, in case of the 2.25 m long wiggler, the 5 mrad opening is not uniform along all its length: the beginning of the wiggler sees the collimator at a slightly smaller angle than its end. Moving the wiggler back- or forwards (so for example its center, instead of its beginning) is aligned with the dipole would change the results slightly.
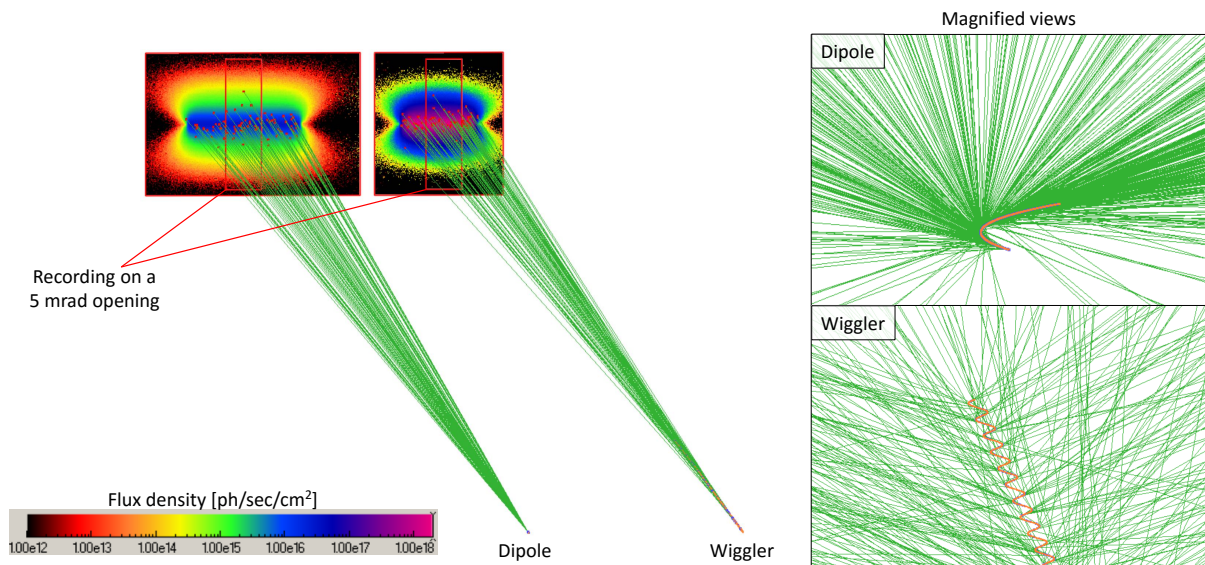
Figure 15: Synrad+ simulation of the VUV bending magnet and the U13U wiggler
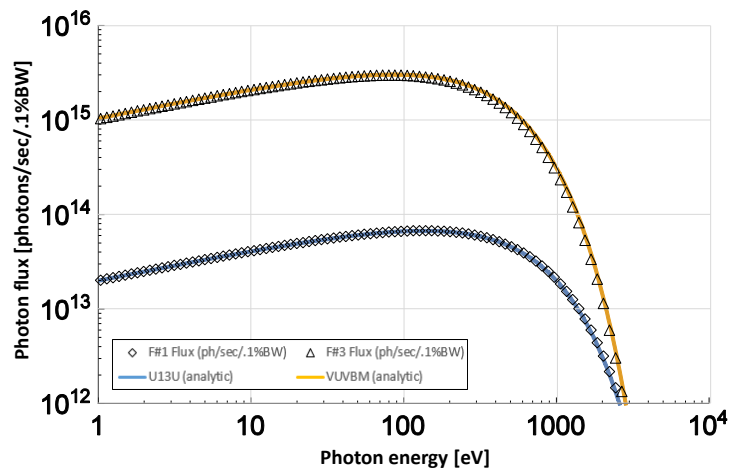

Figure 16: SR spectrum of the VUVBM bending magnet and the U13U wiggler of the VUV Storage Ring of Brookhaven National Laboratory, as calculated by Synrads spectrum plotter tool and as calculated analytically
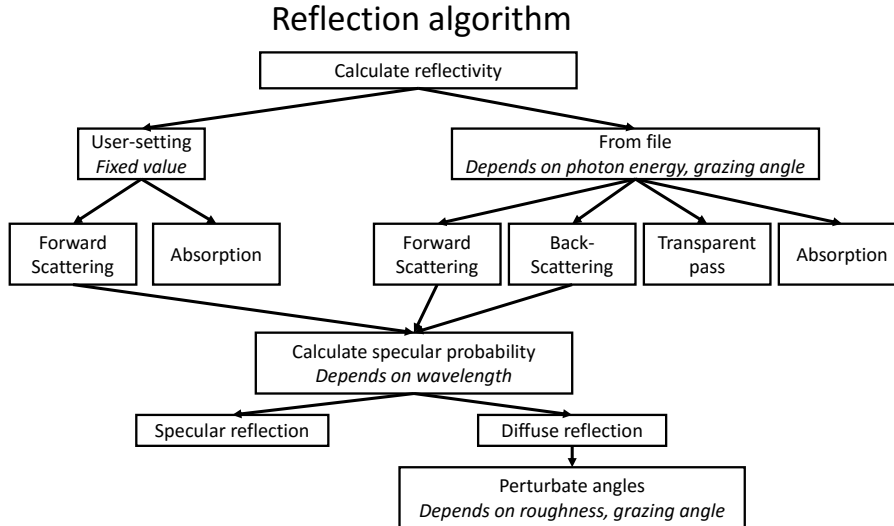
Figure 17: Reflection algorithm main steps in Synrad+

5 Photon tracing

Once virtual photons are generated from a source, they are traced until they are absorbed or until they leave the modeled region. Therefore, at every collision with a surface, reflectivity and photon scattering must be taken into account. Both photon reflectivity and scattering from metallic surfaces are well-established subjects. Many approaches exist to simulate them, from solving the Maxwell equations to different levels of approximations, which in turn are faster to calculate. As our Monte Carlo codes aim for possibly thousands or even millions of simulated hits per second on standard PCs, and usually a geometry consists of thousands of facets, I chose methods which are acceptably accurate on a macroscopic scale, at the same time dont slow down photon tracing excessively.

5.1 Photon reflection

Synrad+ uses the same raytracing engine as Molflow+. However, whereas in vacuum simulations reflection is usually executed simply (Lambertian reflection, optionally with a sticking factor), in case of photons, the model, overviewed in Fig.17 is more complex. Its steps are detailed as follows:

Upon collision with a surface, a virtual photon can be absorbed, transmitted or reflected. In Synrad+ it is possible to define surfaces where these probabilities are user-defined constants (for example, 70% of the incident photons are absorbed, the rest reflected). I consider these cases to be straightforward to implement therefore I dont detail them here.

For a real metal vacuum chamber surface, the reflection probability depends on the material itself, but also on the wavelength (energy) and incident angle of the photon. The idea is that for each material, we store a table of reflection probabilities for a range of photon energies and incident angles, and we interpolate the exact value at each collision.

The model to construct such material tables is described in [18], and can be summarized as follows:

The refractive index of a metallic surface, a complex number, can be calculated from the atomic scattering factors as[14]:

$$n = \frac{r_e}{2\pi} \lambda^2 n' f(0) \tag{4}$$

Where r_e is the classical electron radius, λ is the wavelength, and n' is the number of atoms per unit volume. The complex atomic scattering factor can be expressed as

$$f(0) = f_1 + if_2$$

Where the imaginary part f_2 is derived from the atomic photoabsorption cross section, and the real part f_1 can be obtained from the imaginary part through the Kramers-Kronig dispersion relation. I obtained these factors from the Henke database [19] which contains these scattering factors for most elements of the periodic table for energies between $30\,\mathrm{eV}$ and $30\,000\,\mathrm{eV}$ in a downloadable format.
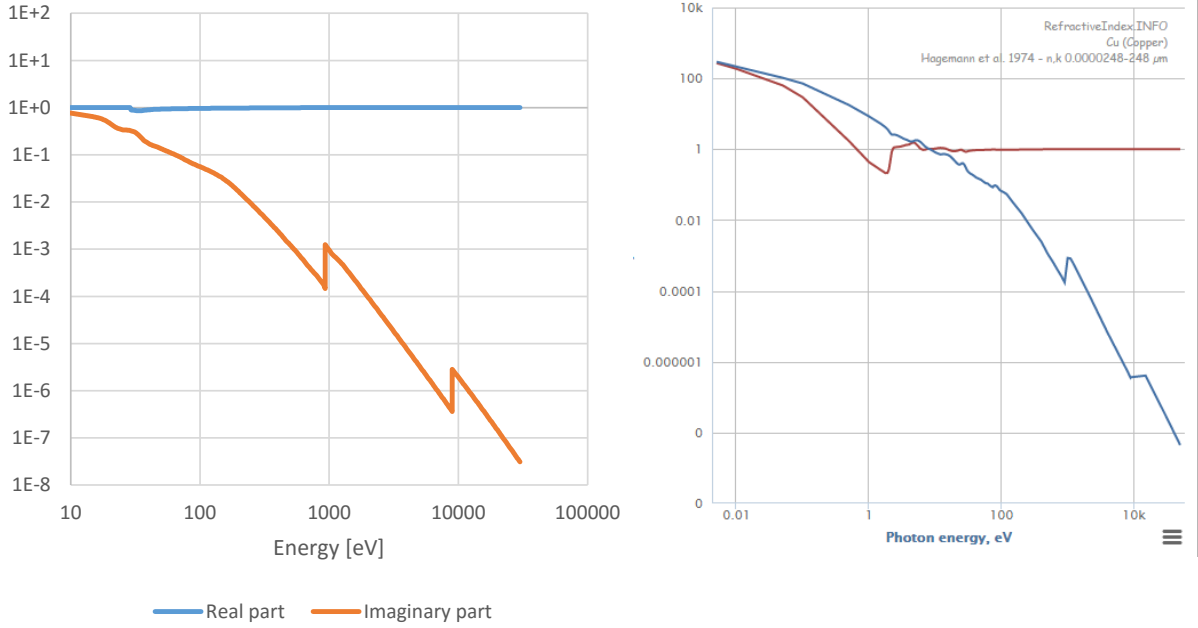
---

[14] See Eq.1 of chapter 1.7 of [18]

Figure 18: Real and imaginary components of copper refractive index
Left: Calculated from eq.4
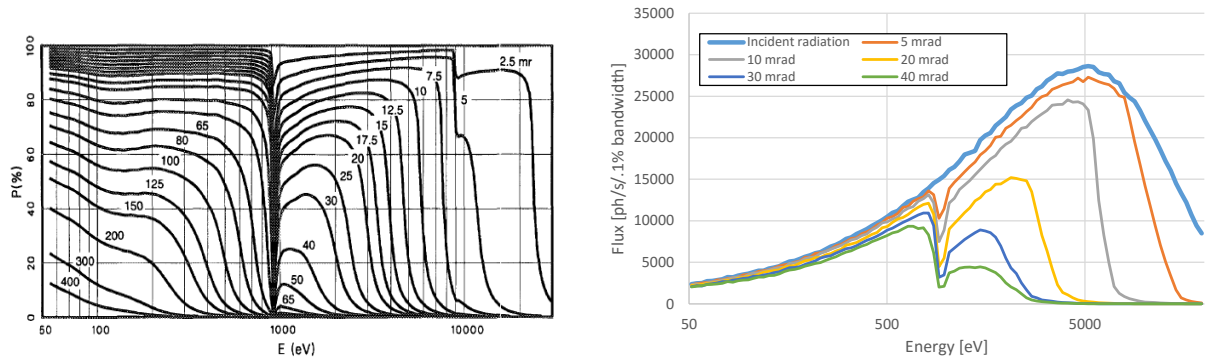Right: As presented on [21], containing data for low energies as well

Figure 19: Copper reflectivity tables for different grazing angles (left) from [19] and Synrad-simulated reflections (right) of SR from a dipole on a copper surface at different grazing angles

As for energies below $30\,\mathrm{eV}$ (important for accelerator applications), I extend our refractive index database for common vacuum materials from [20]. It is worth mentioning that at the moment of writing, there is a significant effort to organize reflection data for many elements originating from various scientific papers, and present them with references in an interactive and downloadable format on a website [21].

With the refractive index at hand (example in Fig.18), we can derive the reflectivity values using the Fresnel formulas:

$$R = |r|^2 = \left| \frac{k_{iz} - k_{tz}}{k_{iz} + k_{tz}} \right|^2$$

Where $k_{iz} = \frac{2\pi}{\lambda}\cos\theta$ and $k_{tz} = \frac{2\pi}{\lambda}\sqrt{n^2 - \cos^2\theta}$

Using the method above, I built a library of reflectivity tables for common materials, such as the one plotted in Fig.19 for copper, and stored it in Synrad+. I also let the user add his own materials through CSV-formatted input files.

These input files apart from the reflectivity - also allow to specify a probability for photon backscattering and transparent pass, useful in two special cases.
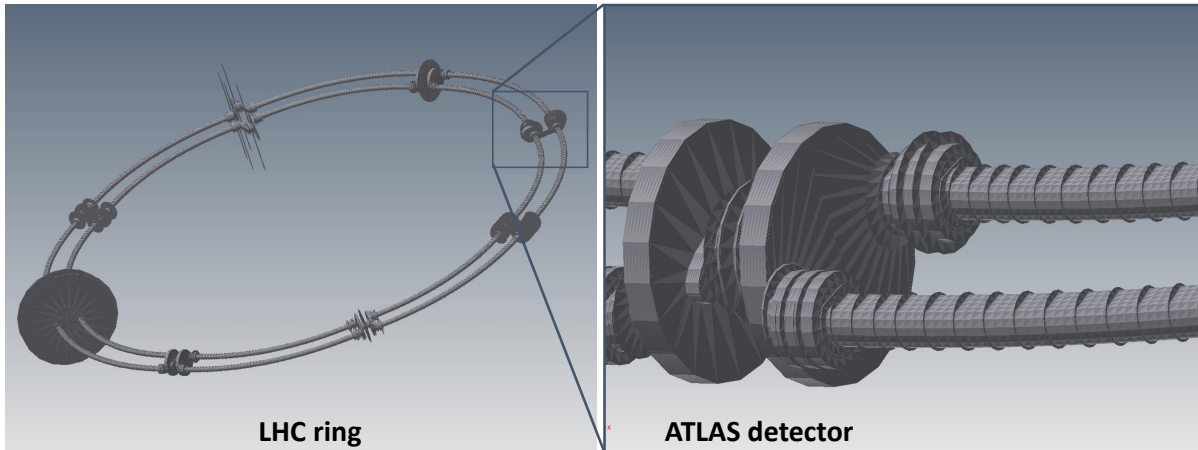
Figure 20: The vacuum system of the LHC ring (left) and the ATLAS detector (right), in a Synrad-importable geometry format. Horizontal distances between the beam pipes increased for visibility. Images: Jan Sopousek (Brno University, CERN)
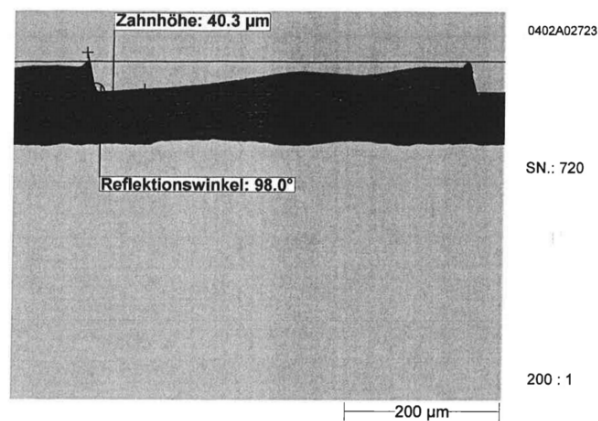

Figure 21: Microscopic surface view of the LHC beam screen, measurements by Nicolaas KOS (CERN)

5.1.1 Sawtooth surfaces

When Synrad+ was used for a photon flux calculation problem in the LHC, the whole, 27 km long vacuum chamber was imported, consisting of 200.000 facets and 2500 magnetic regions (each LHC dipole appeared as two different sources in the two beampipes). The geometry, containing only the vacuum-related parts, is shown for illustration in Fig.20.

The memory usage at this point was approximately 2 GB. The LHC beam screen has a sawtooth profile (of 40 μm height and 500 μm pitch, as in Fig.21) on a 14 mm-high strip centered on the plane of the orbit, where practically all primary photons hit: since, as explained before, photons with near-orthogonal incidence have low scattering probability, this geometry significantly reduces scattering of SR photons down the beamline[22].

In theory, we could describe these surfaces without approximations, i.e. using one polygon for each sawtooth period. However, this would prevent us from simulating such large structures. In our case, modeling each saw-tooth indentation would increase the number of facets to 108 million (LHC length divided by sawtooth period), which is impossible to keep in memory, and even if we could, ray tracing would be extremely slow.

Therefore, to treat this problem, the need came to describe such periodic surfaces with a single facet, and to include the forward- and backscattering through input files.

The forward- and backscattering probabilities can be determined by simulating a simple reflectivity measurement (see Fig.22). 20 magnetic regions, representing quasi-straight dipoles of the same parameters, emit photons of 10 eV with 20 different grazing angles increasing in logarithmic steps.

Each region is separated from the others by opaque facets, so the emitted photons can either be
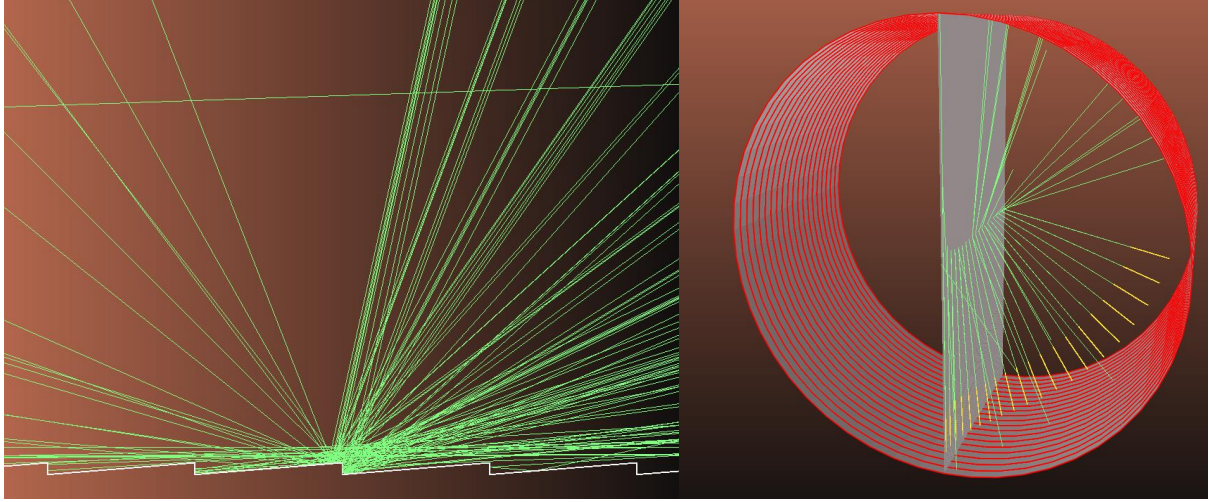
19

Figure 22: Sawtooth surface model and reflectivity measurements in Synrad+.
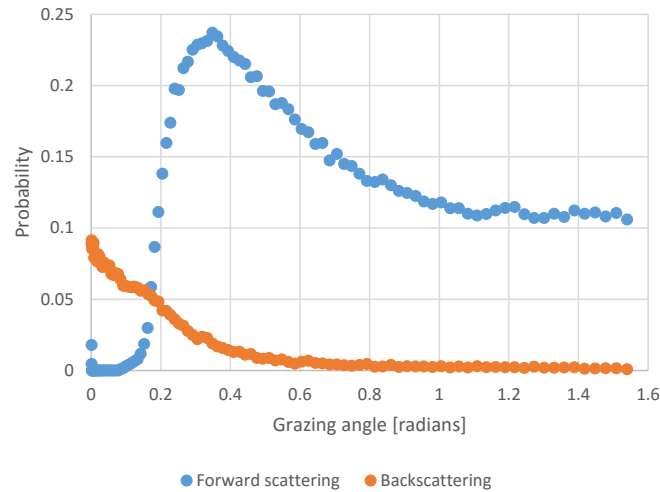Geometry: Jan Sopousek

Figure 23: Simulated forward- and backscattering probabilities of 10 eV photons from a copper sawtooth surface

absorbed on the periodic sawtooth surface, or get reflected forward or backwards. The sawtooth surface is assumed to be made of copper, applying the corresponding reflectivity table.

The forward- and backscattered photons are summed by textures on the target hemispheres, and the ratios are summarized in Fig.23.

Having determined these values, we can repeat the experiment for different photon energies. With these data, we can finally define the sawtooth beam screen as a special surface, described by a single facet, where the input file contains not only single-value reflection probabilities, but for each energy and grazing angle there is a probability for absorption, forward- and backscattering.

We can see in Fig.24 that replacing the periodic structure by such a facet, the reflection pattern is nearly identical in the real and the approximated case.

One notable difference is that the real surface allows backscattering via two different geometrical paths, which is visible through a bifurcation of the scattering pattern for low angles. Also, because the teeth of the surface are tilted compared to the general wall direction, the reflected patterns have some offset.
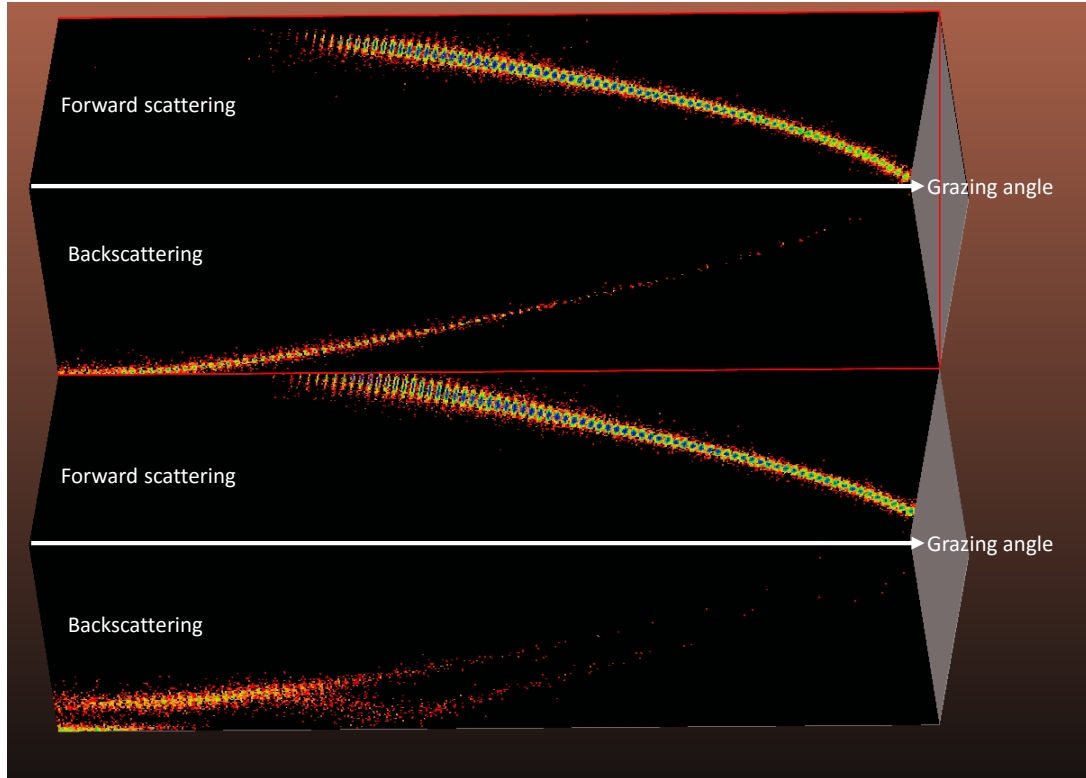
Figure 24: Reflected SR pattern from a sawtooth surface (bottom) and from its approximation as a single facet (top), with different grazing angles, increasing to the right

5.1.2 Transparency

Once our input files can contain several reflection components for each grazing angle and photon energy, it is straightforward to extend the absorption, forward- and backscattering probabilities with a fourth one: transparency. This allows modeling of vacuum windows made of Beryllium, for example. Such a window is partially transparent to synchrotron radiation, but seals the vacuum chamber from the atmosphere.

In the example below, we perform a simple radiation protection calculation, where we calculate how much SR can get out from an aluminum vacuum chamber of 1 cm thickness.

First we obtain and digitize the aluminum mass attenuation coefficient for X-ray wavelengths from the NIST material database (Fig.25). This graph is adjusted to include the Compton effect and pair production for higher energies.

To get the ratio I/I_0 of the incident radiation that traverses the aluminum, we use the equation

$$I = I_0 \exp\left(-\frac{\mu}{\rho}x\right)$$

where $\rho = 2.69\,\mathrm{g\,cm^{-3}}$ is the aluminum density, and

$$x = \frac{1\mathrm{cm}}{\sin\theta}$$

is the path the X-rays travel in the aluminum wall (θ is the grazing angle).

With this information, we can fill all cells of the input file, each describing the ratio of transmitted light for a given energy and grazing angle. The resulting transmission probability file is plotted in Fig.26.

Our simulation (Fig.27) will measure the radiation that originates from a dipole and can escape from a vacuum chamber. The chamber has a diameter that is reduced by a taper after the dipole. Three targets are placed to measure the radiation outside the chamber: (1) placed just after the dipole, (2) after the taper and (3) after the end flange that closes the chamber.

Since aluminum is almost perfectly opaque below energies of 10 keV, I have chosen beam and dipole parameters to include high energies that fall in the semi-transparent region. Simulation parameters are summarized in Table3.
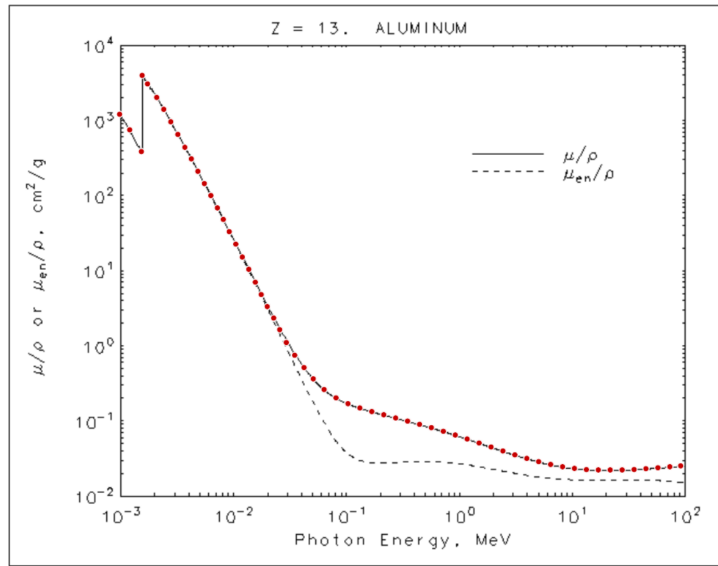
Figure 25: Mass attenuation coefficient of Aluminum, downloaded from NIST database[23], and the data points (in red) show the digitized data points.
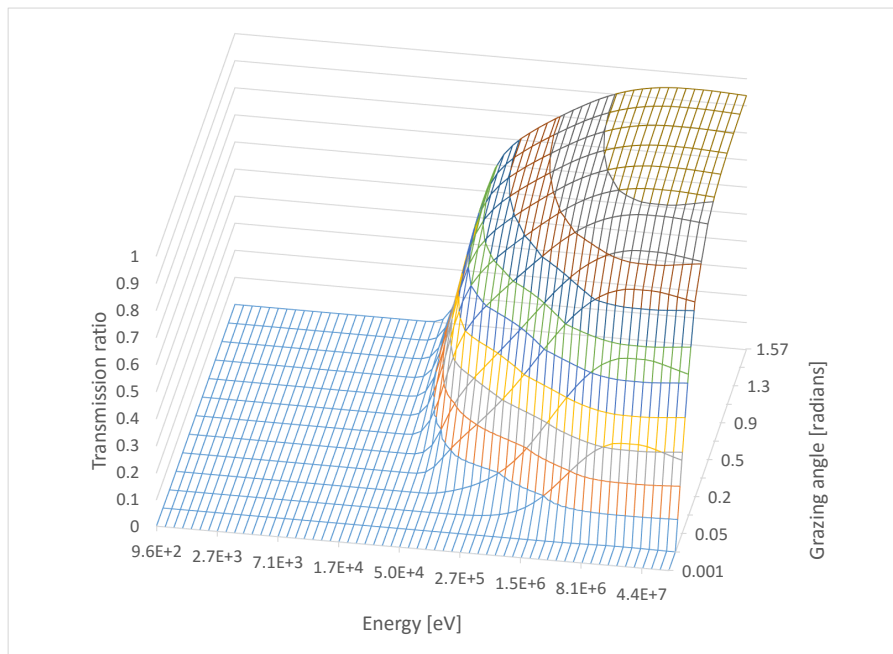

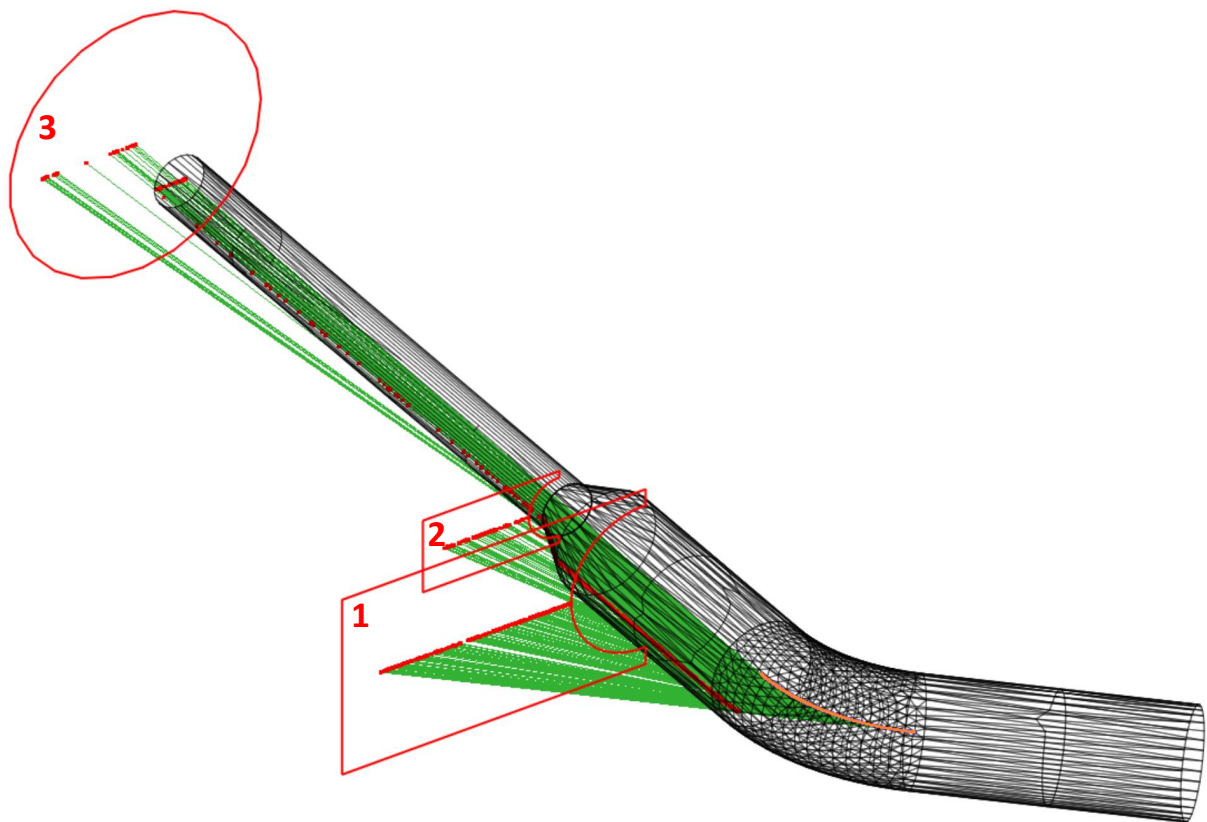Figure 26: Transmission probabilities of X-rays through 1 cm of aluminum

Figure 27: Synchrotron radiation photons (green lines) originating from a 10 GeV beam (orange) bent by a 15.6 T dipole escaping from a 1 cm thick aluminum chamber. External targets are marked with red outlines; photon absorption locations are marked with red dots.

Table 3: Radiation protection example simulation parameters

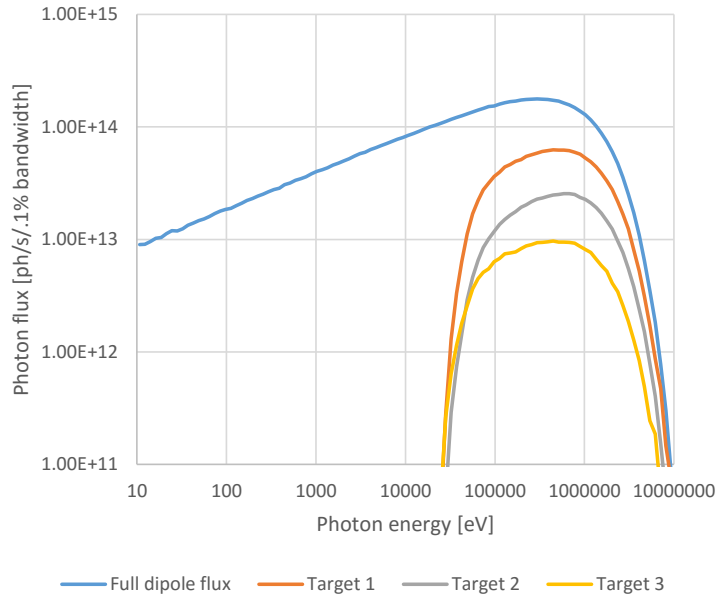| Beam	10 GeV, electrons
Dipole magnetic field	15.6 T
Radius of curvature / critical energy	2.138m / 1MeV
Photon generation range	10eV .. 10 MeV
Photon flux / power	1E18 ph/s, 52.5kW
Virtual photons generated	3 Million
Simulation time (avg. desktop PC)	30 seconds

Figure 28: Transmitted spectrum results on the three targets of the radiation protection simulation

Results show that 29% of the dipole's flux and 62.4% of the power can escape the vacuum chamber. Since aluminum is more transparent at higher photon energies, the power ratio is as expected higher. This is also visible on the spectrums recorded in the targets (in Fig.28).

5.2   Rough surface scattering

Many approaches exist for simulating photon reflection from rough surfaces. In general, these can be classed into:

- Geometric optics methods, which either describe the actual surface with very high detail, or generate it according to a statistical distribution, then perform geometric ray tracing treating the surface points as locally smooth. Usually these methods require storing (or generating on-demand) a large number of polygons for a single surface, which isnt suitable for our simulations which already use a large number of facets for the description of the accelerator geometry.

- Physical optics methods, based on electrodynamics, describing diffuse scattering based on the Maxwell equations. The theory of diffuse scattering of EM waves from random rough surfaces is described in detail in [24] and [25]. These methods are generally too expensive computationally to include in a Monte Carlo simulation where thousands of collisions are expected to be simulated every second.

My code uses therefore a mixed method that is based on a model presented in [26], applied in the synchrotron radiation simulator Synrad3D, developed at Cornell University. That model uses the scalar Kirchhoff theory [27],[28].

The statistical description of the surfaces assumes Gaussian distribution for the surface height variations (of rms σ) and also for the transverse distribution (with autocorrelation coefficient T). Although

the code is closed-source, the mathematics behind it is published. I decided to implement it as Synrad3D is an etalon in the electron-cloud community since several years to estimate the seeding position of photoelectrons [29]. I have, however, applied approximations and optimizations to the model to bring it to a speed that is acceptable for our simulations.

The theory, as described in [30] is as follows:

Upon colliding with a surface, a photon can be absorbed or reflected. The reflection probability of the surface is determined the same way as with smooth surfaces, using the database for materials, as described earlier in this section. If a photon is reflected, there is a certain probability that it does it specularly. In this case, to get the new direction, we mirror the incident direction to the reflecting surface. This specular probability is described by the Debye-Waller factor:

$$P_{spec}\left(y,\lambda\right) = \exp\left[-\left(\frac{4\pi\sigma y}{\lambda}\right)^2\right]$$

In this expression $y = cos(\theta_{in})$, with θ_{in} the angle between the incident direction and the surface normal, λ is the photons wavelength and σ is the RMS surface roughness.

If based on the probability above - a reflection isnt specular, we apply the diffuse scattering model, where the probability of a certain combination of the incident, outgoing and out-of-plane angles are described by the equations:

$$\frac{dF_{diff}}{d\Omega} = \frac{J\left(y,\lambda,x,\phi\right)}{J_0\left(y,\lambda\right)}$$

$$J\left(y,\lambda,x,\phi\right) = \frac{\left(1+xy\right)^2}{\left(x+y\right)^4}\left(1-a\cdot\cos\phi\right)^2 g e^{-g}\sum_{m=1}^{\infty}X_m$$

$$g = \left(\frac{2\pi\sigma\left(x+y\right)}{\lambda}\right)^2$$

$$x_m = \frac{gm}{m!m}e^{-gq/m}$$

$$q = \frac{\left(2-x^2-y^2-2h\cos\phi\right)\tau^2}{4(x+y)^2}$$

$$\tau = \frac{T}{\sigma}$$

$$h = \sqrt{1-(x^2+y^2)+x^2y^2}$$

$$a = \frac{h}{1+xy}$$

In these expressions, $x = \cos\left(\theta_{out}\right)$ is the cosine of the reflected directions angle with the surface normal, and ϕ is the "out of plane" angle, i.e. the angle of the reflected direction with the plane defined by the incident and surface normal vectors.

As mentioned in [30], these expressions simplify in the $g(\sigma,\lambda) >> 1$ limit corresponding to technical vacuum chambers and to high energy photons, for which typically $\sigma >> \lambda$. In this limit, the distribution can be described without the infinite sum:

$$\frac{dF_{diff}}{d\Omega} \simeq \frac{J_a\left(y,x,\phi\right)}{J_{a0}\left(y\right)}$$

where

$$J_a\left(y,x,\phi\right) = \frac{\left(1+xy\right)^2}{\left(x+y\right)^4}\left(1-a\cdot\cos\phi\right)^2 e^{-q}$$

$$J_{a0}\left(y\right) = \int_0^1 dx \int_{-\pi}^{\pi} d\phi J_a\left(y,x,\phi\right)$$

As a compromise between the speed and accuracy, my code uses this high energy approximation (it would be numerically impractical to calculate an infinite sum at every photon reflection with an acceptable speed). However, even this approximation uses a formula that consists of too many mathematical
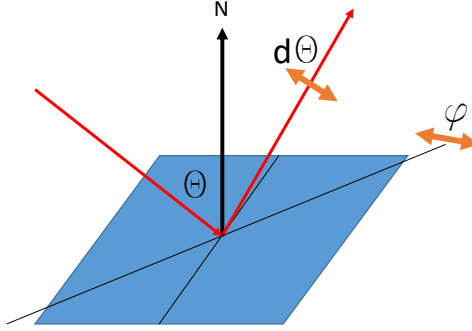
Figure 29: Angle notation for the reflection model in Synrad+

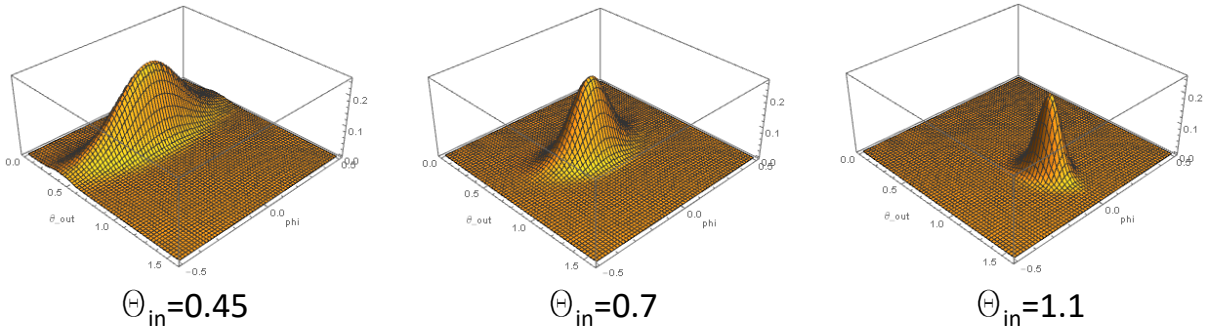Θ_{in}=0.45 Θ_{in}=0.7 Θ_{in}=1.1

Figure 30: Diffuse reflection directional distributions for 3 different θ_{in} incident angles at $\tau = 30$

operations to evaluate efficiently (four power operations, two multiplications, three sums and one trigonometric function - and the integral for all angles). By plotting the distributions, however, it is possible to notice their characteristics that give way to simpler, analytic approximations.

We are interested in the scattering angle $d\theta = \theta_{out} - \theta_{in}$ and the out-of-plane angle ϕ, shown in Fig.29.

Plotting the diffuse part of the scattered distributions on the $\theta_{out}\phi$ plane (Fig.30), we can notice that the distributions are Gaussian-like, with a different width in the two angular directions, and the peak is at the specular reflection point ($\theta_{out} = \theta_{in}$,$\phi = 0$).

I have therefore approximated these distributions as bivariate Gaussians, and made an attempt to describe the standard deviations for both angles analytically, as a function of the roughness ratio τ and the incident angle θ_{in}.

To determine the standard deviations, for each θ_{in} incident angle, I have used a root finding algorithm to find the offsets $d\theta$ and ϕ at which the value of the distribution is $\exp(-1/2) \sim 60.6\%$ of the peak value (Gaussian distributions have this value at their 1σ offset).

Results show that the width of the $d\theta$ distribution is the same for all incident angles, and depends only on the surface roughness, described in our case by the parameter τ. We get the best fit if we choose a Gaussian with $\sigma_\theta = C/\tau$, which has the physical meaning that the more the surface is rough, the wider our angular distribution becomes for the scattered photons.

As for the out-of-plane angle ϕ, the case is more difficult, as the width of the distribution depends on the incident angle and the surface roughness. The dependence on the latter can be quickly found to be similar to the scattering angle, $\sigma_\phi \sim 1/\tau$.

Executing the root-finding algorithm for 100 distinct θ_{in} values shows (Fig.31) that the width of the ϕ distribution shows a near-hyperbolic dependence on the incident angle, suggesting to try fitting with an analytic function similar to $\sigma = A * \sigma^{-1} * \tau^{-1}$. Using the best fit for parameter A, a second fitting run, introducing a correction factor added to the hyperbolic term has resulted in a very accurate fit, as seen on Fig.31. The final solution is summarized in Table4.

Comparing the original distribution with our Gaussian approximations shows practically perfect match for most incident angles. The exception is the when the incident photons are almost parallel to the surface ($1.55 < \theta_{in} < \pi/2$) where the shape of the out-of-planes distribution is somewhat different (Fig.32).

This discrepancy could be solved by fitting a higher order expression or by fitting different functions

$$\sigma_\phi = \frac{2.80657 * \theta^{-1.00238} - 1.00293 * \theta^{1.2266}}{\tau}$$
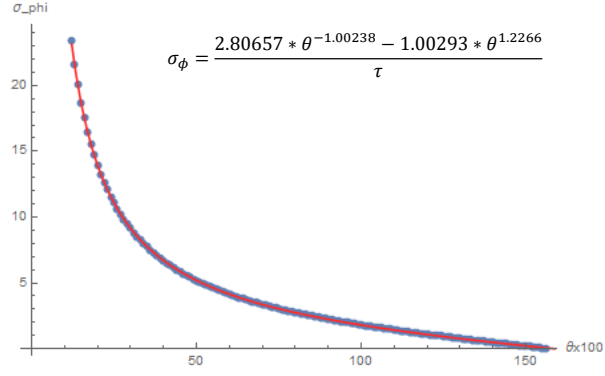
Figure 31: Standard deviation of the reflected SR light's out-of-plane angle distribution, as a function of the incident angle θ_{in}
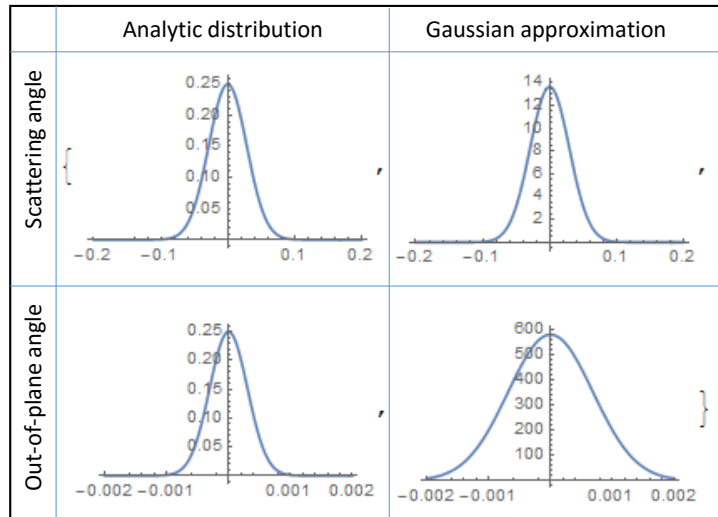

Figure 32: Angular distributions of the analytic expressions, as published in [30] and their Gaussian approximations in Synrad, for a near-parallel incidence $\theta_{in} = 1.56$ and $\tau = 100$

Table 4: Fit parameters for the reflection angles

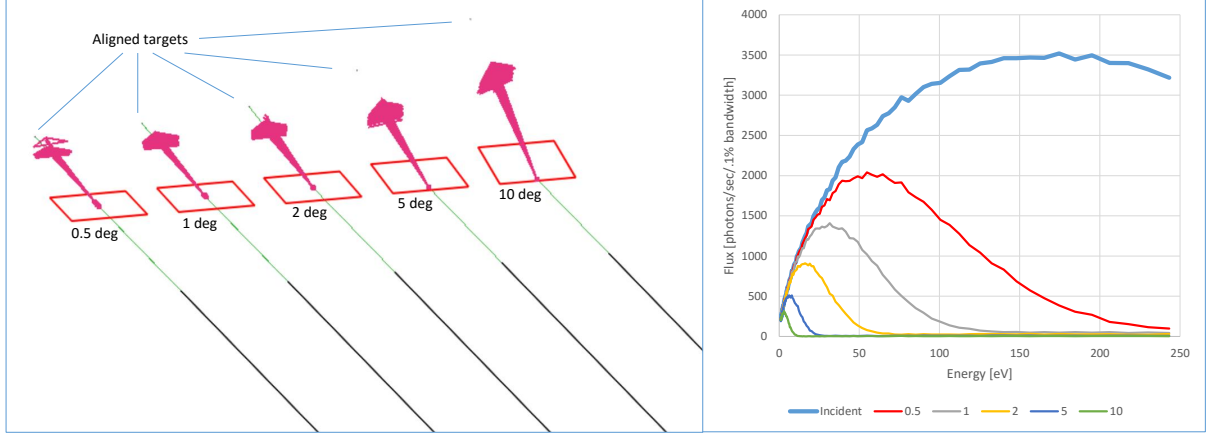| Scattering angle θ_{out}	Gaussian, mean=θ_{in} $\sigma_\theta = \frac{2.9267}{\tau}$
Out-of-plane angle ϕ	Gaussian, mean=0 $\sigma_\phi = \frac{2.80657*\theta^{-1.00238}-1.00293*\theta^{1.2266}}{\tau}$

Figure 33: Specular reflectivity test in Synrad+

for different domains of the incident angles. As these practices would cost computation time for all incident angles, I have decided to not implement them for the moment.

5.3 Validation

As results of the model I approximate are published in [30], a practical benchmarking of my approximation can be done by simulating a reflectivity measurement in Synrad+. I set up five identical dipole sources, each surrounded by a long and narrow tube. The highly collimated SR light exiting the tubes was then projected to surfaces tilted at different angles.

5.3.1 Specular reflectivity

At this test, the five reflective surfaces were placed so that the grazing angle of the incident photons were 0.5, 1, 2, 5 and 10 degrees, respectively. I calculated the specular part of the reflected light by placing and carefully aligning five very small targets in the specular direction. That way the diffusely reflected light, which is distributed over a larger solid angle misses the targets, so measuring the spectrum on the targets gives us information of the specular part[15]. Simulation parameters are summarized in Table5 and an overview is shown in Fig.33.

Having the spectrum of the incident flux and the specularly reflected photons at each target, for every photon energy, we can calculate the specular reflection ratio. This allows comparison with published data from Fig.2 of [30]. As shown in Fig.34, the simulated ratios match reasonably well with the Debye-Waller

---

[15]Strictly speaking, the small targets in the specular direction also collect the peak of the diffuse part, however my measurements show that its flux is negligible compared to the specular flux.

Table 5: Synrad+ simulation parameters for the specular reflectivity test

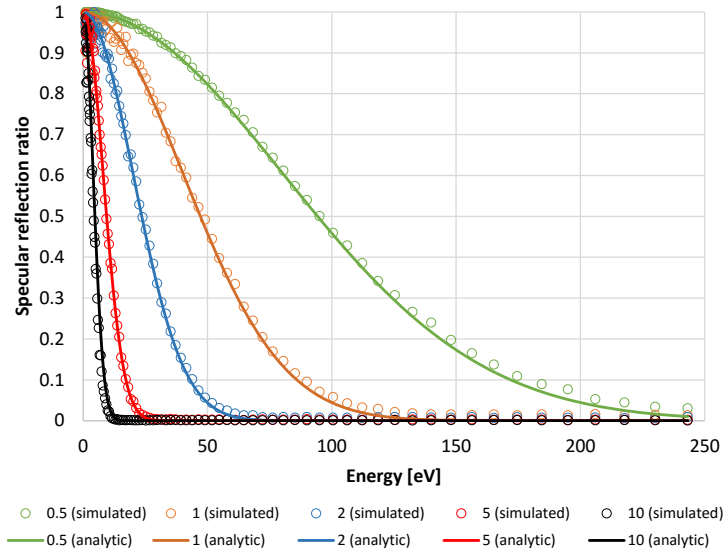|	
Beam	1 GeV, electron, 1 mA
Dipole	0.3T, 1 mm length
Collimators	20 cm length, 10 μm diameter
Surface roughness	σ=100 nm, τ=100
SR generation	1..250 eV, with E_c=199.4 eV
Generated photons	400 million
Photons reaching targets	1 million

Figure 34: Ratio of specularly reflected SR at different grazing angles (in degrees, see legend) of a Synrad+ simulation, compared to the analytic Debye-Waller factor

Table 6: Synrad+ simulation parameters for the diffuse reflectivity test

Beam	3 GeV, electron, 1 mA
Dipole	1 T, 1 mm length
Collimators	20 cm length, 10 μm diameter
Surface roughness	σ=100 nm, τ=100
SR generation	fixed at 6000 eV, with E_c=5983 eV
Generated photons	225 million
Photons reaching targets	2.5 million

factor, except for some imprecisions at very low energies (where the incident flux is low) and high energies (where the reflected flux is low).

5.3.2 Scattering and out-of-plane angles

In this test I measure the angular distribution of the diffusely reflected pattern. Compared to the previous setup, in this case only a fixed energy of the SR spectrum is generated, and the targets are larger, each containing a texture of 1042x201 cells. The reflective surfaces are tilted at 1, 2, 5, 10 and 20 degrees, and the targets are placed exactly 5 cm from the reflection point, so that each texture cell location on their surface can be converted to $d\theta$, ϕ angles by trigonometric formulas (the targets are centered around the specular reflection point).

The test parameters are summarized in Table 6, and the angular distributions are calculated (Fig.36) from the texture values, for comparison with data published in the original article (Figures 5 and 6 of [30]).

Comparison shows the aforementioned discrepancy for low grazing angles, most visible for the out-of-plane distribution for 1 and 2 degrees (my code approximates the distribution to be wider than the analytic solution). For other incident angles the difference is negligible. Depending on the frequency of Synrad+ usage for very low grazing angles, it might be necessary in the future to perform the analytic approximation of the out-of-plane angle by fitting several functions on different domains. That would yield a better match for low grazing angles, at the expense of making the code somewhat slower and more complex.

5.4 Low-flux mode

When presenting my ultra-high vacuum simulations in chapter **??**, I mentioned that large pressure differences cause a problem since for every test particle in the low pressure region, we might need up to
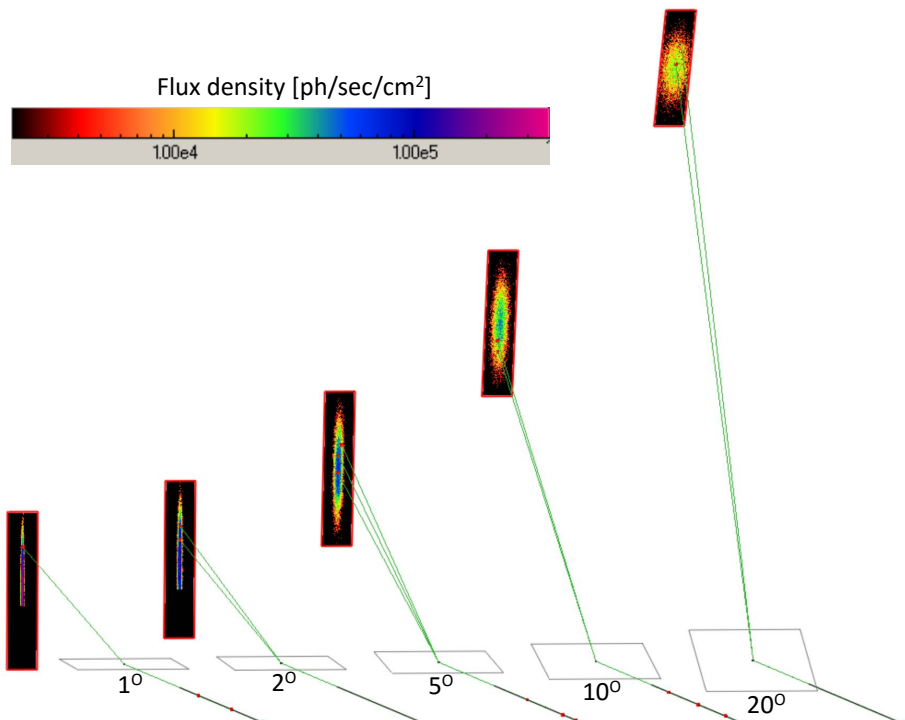
Figure 35: Diffuse reflectivity test in Synrad+
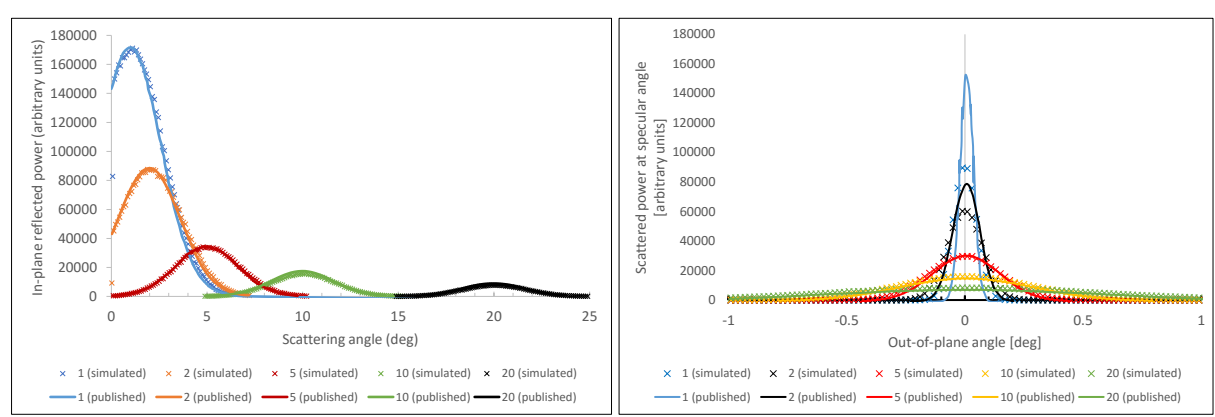

Figure 36: Comparison of scattering angle (left) and out-of-plane angle (right) distributions on a rough surface of $\sigma =$100 nm and $\tau = 100$, for 6 keV photons, simulated by Synrad+ and as published in Figures 5 and 6 of [30]
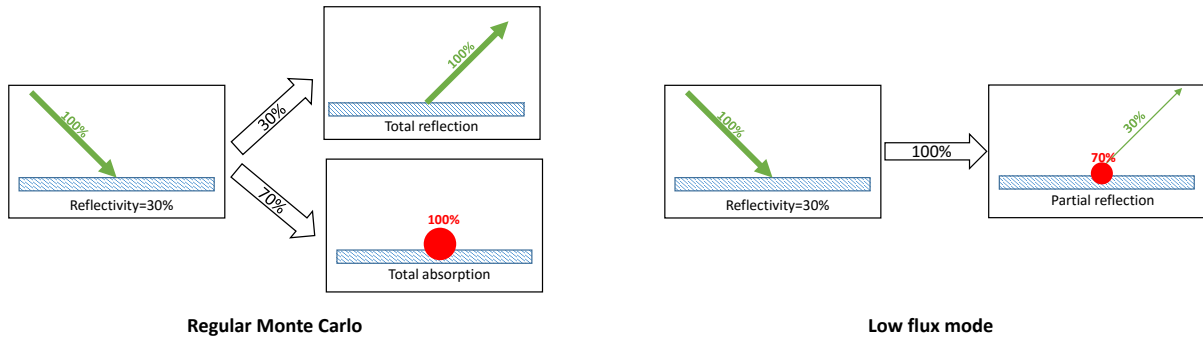
Figure 37: Synrad+ low flux mode overview

thousands of traced particles in high pressure regions.

We face a similar problem during SR simulations: as described later in chapter **??**, in some cases we need to simulate 7 orders of magnitude of flux density. In such a case, for a single Monte Carlo hit in the low flux regions, 10 million test photons are traced in the high-flux parts.

A way to mitigate this problem is to dynamically change the represented photon flux of a test photon as we trace it in our system. When a test photon is generated, it represents a certain number of real photon flux, the exact number expressed in eq.2. When this test photon hits a reflective surface, there is a certain probability that it will be reflected, otherwise it will be absorbed locally. Our random generators assure that the ratio of reflected photons will match the surface reflectivity.

If this reflectivity is small, for example 10%, then the chance of - lets say - 5 consecutive reflections is very low ($0.1^5 = 0.00001$), meaning that to register a single hit on areas reachable only by 5 or more reflections, 100.000 test photons are required on average.

We can therefore change the algorithm and as shown in Fig.37 do ray-tracing in such a way that the photon is always reflected, but after the reflection the real flux it represents is reduced. If R is the surface reflectivity, and F_{in} is the photon flux it represents at incidence,

- the photon will be reflected, and the outgoing photon will represent $F_{out} = R * F_{in}$ flux of real photons

- and $(1 - R) * F_{in}$ absorbed flux will be registered at the reflection point (in form of textures, etc.)

In this case, however, we must assure that the ray-tracing eventually stops. I let the user define a cutoff ratio. If the ratio of the test particles actual representation (reduced through multiple reflections) and the original representation falls below this cutoff ratio, we eliminate the photon.

As a thumb rule, if the user is interested in N orders of magnitude of flux density, then the optimal cutoff ratio is 10^{-N}.

This low flux mode was implemented for the simulation of low-flux areas of the SuperKEKB interaction region (see section **??**). We were interested in 9 orders of magnitude of flux density, calculations often requiring overnight simulations. In Fig.38 the result of this low-flux mode (with cutoff ratio of 1E-7) is compared to the standard algorithm after 3 million traced hits.
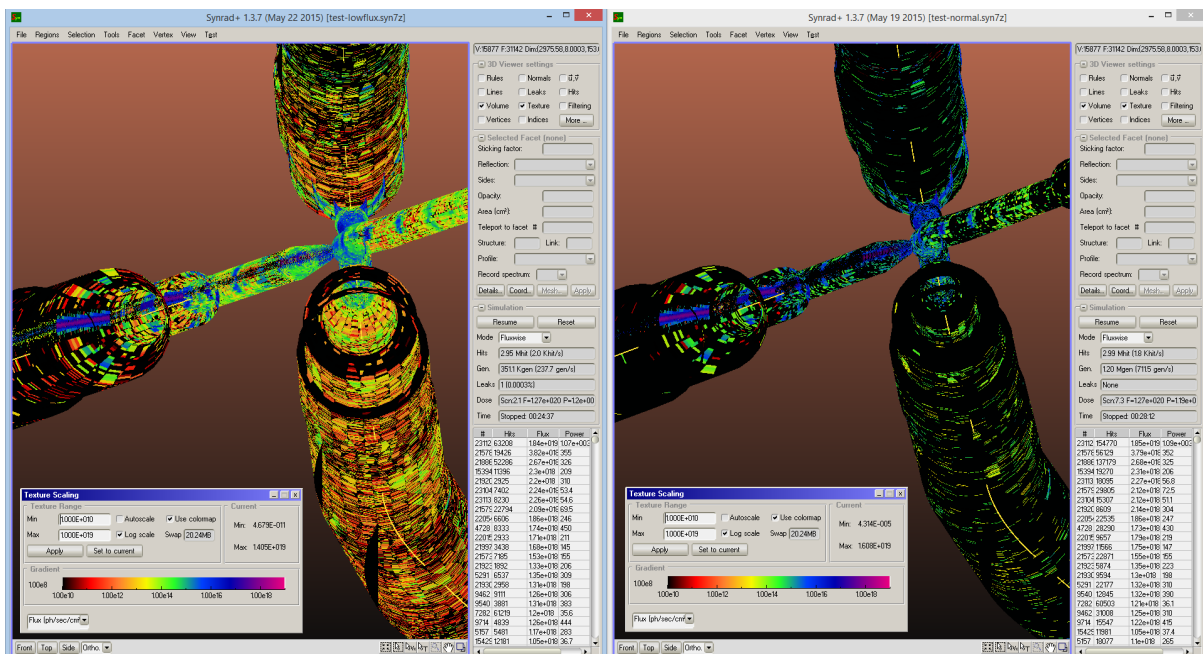
Figure 38: Flux density of the SuperKEKB interaction region, after 3 million Monte Carlo hits, simulated with low-flux mode enabled (left) and disabled (right), shown on the same color scale. While flux density values are exactly the same for high-flux areas (blue/violet colors), low-flux areas (red, yellow) have significantly more statistics with the low-flux mode enabled.

References

[1] Marton Ady, Roberto Kersevan, and Rivkin Leonid. *Monte Carlo simulations of ultra high vacuum and synchrotron radiation for particle accelerators.* PhD thesis, Ecole Polytechnique, Lausanne, May 2016. Presented 03 May 2016.

[2] R. Kersevan. Synrad, a monte carlo synchrotron radiation ray-tracing program. In *Particle Accelerator Conference, 1993., Proceedings of the 1993*, pages 3848–3850. IEEE, 1993.

[3] J Rossbach and Peter Schmueser. Basic course on accelerator optics. In *Conf. Proc.*, volume 9209071, pages 17–88, 1992.

[4] GK Green. Spectra and optics of synchrotron radiation. Technical report, Brookhaven National Lab., Upton, NY (USA), 1976.

[5] J.D. Jackson. *Classical electrodynamics.* Wiley, 1999.

[6] K.T. McDonald: Notes on Synchrotron Radiation, Princeton U., Feb 10 1997.

[7] H H Umsttter. Efficient computation of synchrotron radiation spectrum. Technical Report CERN-PS-SM-81-13, CERN, Geneva, 1981.

[8] H Burkhardt. Monte Carlo generation of the energy spectrum of synchrotron radiation. Technical Report CERN-OPEN-2007-018. CLIC-Note-709. EUROTEV-Report-2007-018, CERN, Geneva, Jun 2007.

[9] A. Hofmann. *The Physics of Synchrotron Radiation.* Cambridge Monographs on Particle Physics, Nuclear Physics and Cosmology. Cambridge University Press, 2004.

[10] J. Schwinger. On the classical radiation of accelerated electrons. *Physical Review*, 75(12):1912, 1949.

[11] S Mobilio and A Balerna. Introduction to the main properties of synchrotron radiation. In *Conference Proceedings-Italian Physical Society*, volume 82, pages 1–24. Editrice Compositori; 1999, 2003.

[12] Do H Tomboulian and PL Hartman. Spectral and angular distribution of ultraviolet radiation from the 300-mev cornell synchrotron. *Physical Review*, 102(6):1423, 1956.

[13] A.A. Sokolov and I.M. Ternov. Synchrotron radiation. *Akademia Nauk SSSR, Moskovskoie Obshchestvo Ispytatelei prirody. Sektsia Fiziki. Sinkhrotron Radiation, Nauka Eds., Moscow, 1966 (Russian title: Sinkhrotronnoie izluchenie), 228 pp.*, 1, 1966.

[14] R. Coisson. Angular-spectral distribution and polarization of synchrotron radiation from a "short" magnet. *Phys. Rev. A*, 20:524–528, Aug 1979.

[15] S. Agostinelli, J. Allison, K al Amako, J Apostolakis, H Araujo, P Arce, M Asai, D Axen, S Banerjee, G Barrand, et al. Geant4a simulation toolkit. *Nuclear instruments and methods in physics research section A: Accelerators, Spectrometers, Detectors and Associated Equipment*, 506(3):250–303, 2003.

[16] Madx website. `http://mad.web.cern.ch/mad/`. Accessed: 2016-02-28.

[17] Steven L.H. and Jill M.W. Flux and brightness calculations for various synchrotron radiation sources. *Nuclear Instruments and Methods in Physics Research Section A: Accelerators, Spectrometers, Detectors and Associated Equipment*, 319(13):25 – 31, 1992.

[18] The X-Ray Data Booklet, Lawrence Berkeley National Laboratory, Oct. 2009.

[19] B.L. Henke, E.M. Gullikson, and J.C. Davis. X-ray interactions: Photoabsorption, scattering, transmission, and reflection at e = 50-30,000 ev, z = 1-92. *Atomic Data and Nuclear Data Tables*, 54(2):181 – 342, 1993.

[20] H-J Hagemann, W Gudat, and C Kunz. Optical constants from the far infrared to the x-ray region: Mg, Al, Cu, Ag, Au, Bi, C, and Al2 O3. *JOSA*, 65(6):742–744, 1975.

[21] Refractive Index Database - Mikhail Polyanskiy. `http://refractiveindex.info/`. Accessed: 2016-02-28.

[22] O. Groebner, The Impact of SR in the LHC, VLHC Workshop, 18-20 Sept 2000.

[23] NIST Database. `http://physics.nist.gov/PhysRefData/XrayMassCoef/ElemTab/z13.html`. Accessed: 2016-02-29.

[24] P. Beckmann and A. Spizzichino. The scattering of electromagnetic waves from rough surfaces. *Norwood, MA, Artech House, Inc., 1987, 511 p.*, 1987.

[25] J. A. Ogilvy and Harold M. Merklinger. Theory of wave scattering from random rough surfaces. *The Journal of the Acoustical Society of America*, 90(6):3382–3382, 1991.

[26] G. Dugan and D. Sagan. Synrad3d photon propagation and scattering simulations. 2013.

[27] H. Hogrefe and C. Kunz. Soft x-ray scattering from rough surfaces: experimental and theoretical analysis. *Applied optics*, 26(14):2851–2859, 1987.

[28] RJ Noll and P Glenn. Mirror surface autocovariance functions and their associated visible scattering. *Applied optics*, 21(10):1824–1838, 1982.

[29] G Dugan, M Billing, K Butler, J Chu, J Crittenden, M Forster, D Kreinick, R Meller, M Palmer, G Ramirez, et al. Observations and Predictions at CesrTA, and Outlook for ILC. *arXiv preprint arXiv:1310.0261*, 2013.

[30] GF Dugan, KG Sonnad, R Cimino, T Ishibashi, and F Schäfers. Measurements of x-ray scattering from accelerator vacuum chamber surfaces, and comparison with an analytical model. *Physical Review Special Topics-Accelerators and Beams*, 18(4):040704, 2015.